

1 Quantifying the migration rate of drainage divides from 2 high-resolution topographic data

3 Chao Zhou¹, Xibin Tan^{2,*}, Yiduo Liu², Feng Shi^{1,3}

4 ¹ State Key Laboratory of Earthquake Dynamics, Institute of Geology, China
5 Earthquake Administration, Beijing 100029, China

6 ² Key Laboratory of Mountain Hazards and Surface Processes, Institute of Mountain
7 Hazards and Environment, Chinese Academy of Sciences, Chengdu 610299, China

8 ³ Shanxi Taiyuan Continental Rift Dynamics National Observation and Research
9 Station, Beijing 100029, China

10 *Corresponding author. E-mail address: tanxibin@imde.ac.cn

11 Abstract

12 The lateral movement of drainage divides is co-influenced by tectonics,
13 lithology, and climate, and therefore archives a wealth of geologic and climatic
14 information. Besides, it also has wide-ranging consequences implications for
15 topography, the sedimentary record, and biological evolution, thus has drawn much
16 attention in recent years. -Several methods have been proposed to determine the
17 direction of drainage-divide's migration state (direction and rate), including
18 geochronological field-based approaches investigations (e.g., ¹⁰Becosmogenic nuclides
19 sampling) and topography modeling-based approaches (e.g., χ -plots or Gilbert
20 metrics). A key object in these In the above methods, is the channel head, which
21 separates the hillslope and channel, is an important analysis object. Zhou et al.

22 ~~(2022a) proposed a method to quantify a drainage divide's migration rate using both~~
23 ~~sides' high base-level γ values. However, due to the limited by the resolution of~~
24 ~~topography data, the required channel-head parameters in the calculation often cannot~~
25 ~~be determined accurately, and empirical values are used in the calculation, which may~~
26 ~~induce uncertainties. However, how to quantify the migration rate of drainage divides~~
27 ~~remains challenging.~~ Here, we propose ~~a new~~ two approach methods to calculate the
28 migration rate of drainage divides ~~from high-resolution topographic data. The new~~
29 ~~method is based on the cross-divide comparison of channel head parameters,~~
30 ~~including the critical upstream drainage area and the gradient of channel head, both of~~
31 ~~which are used to calculate the normalized channel steepness at the channel head.~~
32 ~~one is based on the measured~~ relatively accurate channel-head parameters derived
33 from high-resolution topographic data, and the other is based on the improved method
34 of Zhou et al (2022a). We then apply the ~~new~~ methods to an active rift shoulder
35 (Wutai Shan) in the Shanxi rift, and a tectonically stable area (Yingwang Shan
36 mountain range in the Loess Plateau) in the Loess Plateau in North China, to illustrate
37 ~~the calculation of~~ how to calculate drainage-divide migration rates. Our results find
38 show that the divide in the Wutai Shan drainage divide range is migrating
39 northwestward at a rate of between 0.21 to 0.27 mm/yr, whereas the migration rates at
40 the Yingwang Shan in the Loess Plateau are approximately zero. ~~The northward~~
41 ~~migration rates at the Wutai Shan range from 0.10 to 0.13 mm/yr. The migration rates~~
42 ~~are approximately zero at the mountain range in the Loess Plateau. This study~~
43 indicates that the drainage-divide stability can be determined more accurately using

44 high-resolution topographic data. Furthermore, this study takes his study
45 demonstrates that the migration rate of drainage divides can be determined more
46 accurately once the ~~influence of~~ cross-divide differences in the uplift rate of channel
47 heads are taken into account into account in the measurement of drainage-divide
48 migration rate for the first time.

49 **Keywords**

50 Drainage divide; Migration rate; High-resolution topographic data; DEM; Channel
51 head

52 **1. Introduction**

53 The evolution of the Earth's surface is jointly controlled by tectonics, lithology,
54 and climatic conditions (e.g., Molnar and England, 1990; Whipple, 2009; ~~Bonnet,~~
55 ~~2009;~~ Gallen, 2018; ~~Zondervan et al., 2020;~~ Bernard et al., 2021; ~~Hoskins et al.,~~
56 ~~2023~~). ~~This, provides providing~~ a basis for reconstructing the past tectonic (Pritchard
57 et al., 2009; Kirby et al., 2012; ~~He et al., 2021;~~ Shi et al., 2021; ~~Schildgen et al., 2022~~)
58 or climatic processes (Tucker et al., 1997; Hancock et al., 2002; ~~Schildgen et al.,~~
59 ~~2022~~) through topography. The evolution of ~~unglaciated terrestrial terrain~~ topography
60 is fundamentally coupled with changes in drainage systems; ~~including which~~
61 ~~are through~~ river's vertical (~~changes in river long profile~~) and lateral movements
62 (~~drainage divide migration and river captures~~) (Whipple, 2001; Clark et al., 2004;
63 ~~Bonnet, 2009;~~ Willett et al., 2014; ~~Zeng and Tan, 2023~~). Previous studies have

64 extensively investigated how river channel profiles respond to tectonic uplift
65 (Whipple, 2001; Crosby and Whipple, 2006; Kirby et al., 2012; ~~Pritchard et al., 2009;~~
66 ~~Kirby et al., 2012; Goren et al., 2014~~), lithological difference (Duvall et al., 2004;
67 Safran et al., 2005; Forte et al., 2016), and precipitation perturbations (Schlunegger et
68 al., 2011; Bookhagen and Strecker, 2012). ~~Knick points, channel steepness and~~
69 ~~river's long profiles have been used to study the earthquake events (e.g., Burbank~~
70 ~~and Anderson, 2001; Wei et al., 2015); and the spatio-temporal differences-variations~~
71 ~~of uplift distribution (e.g., Whipple et al., 1999; Kirby et al., 201203; Pritchard et al.,~~
72 ~~2009; Goren et al., 2014); and uplift history (e.g., Pritchard et al., 2009; Goren et al.,~~
73 ~~2014). However, r~~Recent studies show that the widespread lateral movement of river
74 basins driven by geological and/or climatic disturbance (Yang et al., 2019; Clark et
75 al., 2004; Deng et al., 2020; Zondervan et al., 2020Zhao et al., 2021; Zhou et al.,
76 2022a; Bian et al., 2024) also interacts with the adjustment of channel profiles (Willett
77 et al., 2014). Drainage-divide migration, one form of river lateral movement~~therefore~~,
78 may not only carry information on geologicalal and/or climatic disturbance (~~Yang et al.,~~
79 ~~2019; Su et al., 2020; Zondervan et al., 2020; He et al., 2021; Shi et al., 2021; Zhou et~~
80 ~~al., 2022a; Zeng and Tan, 2023; Zeng and Tan, 2023~~) but also impact-influence the
81 extraction of tectonic information from channel profiles (Goren et al., 2014; Ma et al.,
82 2020; Jiao et al., 2021). ~~Besides~~Moreover, it also has wide-ranging multi-facet
83 consequences for topography-landscape evolution (Scheingross et al., 2020; Stokes et
84 al., 2022; Scheingross et al., 2020), the sedimentary record processes (Clift &
85 Blusztajn, 2005; Willett et al., 2018; Deng et al., 2020; Zhao et al., 2021), and

86 [biological evolution \(Waters et al., 2001; Zemplak et al., 2008; Hoorn et al., 2010;](#)
87 [Musher et al., 2022\)](#). For this reason, the stability of drainage divides has drawn more
88 and more attention in recent years (e.g., [Authemayou et al., 2018; Vacherat et al.,](#)
89 [2018; Chen et al., 2021; Shelef and Goren, 2021; Sakashita and Endo, 2023; Bian et](#)
90 [al., 2024\)](#).

91 Drainage-divide migration is essentially controlled by the cross-divide
92 difference in erosion [and topographic slope](#) ([Beeson et al., 2017; Dahlquist et al.,](#)
93 [2018; Chen et al., 2021; Zhou et al., 2022a; Stokes et al., 2022\)](#). The erosion rates are
94 routinely derived from geochronological techniques, such as cosmogenic nuclides
95 (e.g., ^{10}Be) concentration measurements ([Mandal et al., 2015; Struth et al., 2017;](#)
96 [Sassolas-Serrayet et al., 2019\)](#), which can be used to calculate the migration ~~velocities~~
97 [rates](#) of drainage divides ([Beeson et al., 2017; Godard et al., 2019; Hu et al., 2021\)](#).
98 However, these techniques are usually based on samples collected from ~~an a~~
99 [catchment](#) outlet that is several, [or even tens of,](#) kilometers away from the drainage
100 divide and thus may not represent the erosion rates close to the drainage divide
101 ([Sassolas-Serrayet et al., 2019; Zhou et al., 2022a\)](#). Besides, the high cost of sample
102 ~~testing processing~~ makes it ~~very~~-challenging to determine the drainage divide's
103 motion by measuring the erosion rates throughout the ~~entire-large~~ landscapes. Hence,
104 it would be ideal to find an accessible and efficient method that can be applied to the
105 entire landscape and ~~cross-checked to~~ make full use of the ^{10}Be -derived erosion rates.

106 The advancement of [the digital elevation model \(DEM\)remote sensing](#)
107 [technology](#) has promoted the development of geomorphic analysis ~~theory~~, making it

108 possible to determine the drainage divide's transient motion through topography
109 analysis. For example, Willett et al. (2014) ~~developed~~ applied the χ method to map the
110 dynamic state of river basins. Forte and Whipple (2018) proposed the cross-divide
111 comparison of "Gilbert metrics" (including channel heads' relief, slope, and elevation)
112 to determine a drainage divide's ~~motion~~ migration direction. Others adopted the
113 comparison of slope angle or relief of the hillslopes across a drainage divide to deduce
114 its stability (Scherler and Schwanghart, 2020; Ye et al., 2022; Zhou et al., 2022b).
115 ~~Although~~ ~~†~~ These geomorphic techniques ~~are quantitative~~, so far, ~~they~~ could only
116 determine the migration direction of drainage divides. ~~No rates have been obtained.~~
117 Braun (2018) ~~raised~~ provided an method equation that considers both alluvial and
118 fluvial areas to calculate the migration velocity of an escarpment (also a drainage
119 divide). Zhou et al. (2022a) developed a technique to calculate the migration rate
120 through the high base-level cross-divide χ ratio of χ values on both sides of a drainage
121 divide ~~high base level channel segments~~. ~~These new above study~~ approaches require
122 channel-head parameters to calculate the migration rate. However, the location of the
123 channel heads sometimes cannot be accurately identified, because of the limitation in
124 limited by the resolution of DEMs in natural cases (e.g., Zhou et al., 2022a). For this
125 reason, empirical values of channel-head parameters are used in these studies
126 above study (Zhou et al., 2022a), which may induce uncertainties. However, the
127 channel head parameter such as the critical upstream area is an empirical value from
128 previous studies, which may not be applicable in specific natural areas and, therefore,
129 could create great uncertainties in the result of migration rates.

130 This study aims to establish an approach to derive the migration rate of drainage
131 divides, at a high precision and low cost, based on topographic analysis. In this study,
132 ~~w~~We choose a tectonically active area, (i.e., the Wutai Shan in the Shanxi ~~rift~~Rift)
133 ~~system,~~ and a tectonically inactive area, (i.e., ~~an unnamed mountain range~~the
134 Yingwang Shan in the Loess ~~plateau~~Plateau), to demonstrate how to quantify
135 drainage-divide migration rates (Fig. 1). We use the aerial photography acquired by
136 unmanned aerial vehicles (UAVs) and the Structure from Motion (SfM) technology to
137 obtain the ~~high-high-resolution topography-DEM~~ data of these two areas (0.67 m and
138 0.84 m spatial resolution in the Wutai Shan and the Yingwang Shan, respectively).
139 Benefiting from the high-resolution data, the location of channel heads can be
140 ~~accurately identified more accurately. Based on the high-resolution data, w~~We then
141 ~~developed~~ two methods to calculate the drainage-divide migration rates. e One is
142 based on the measured channel-head parameters, and the other is based on ~~the an~~
143 improved method of Zhou et al (2022a).first identify the position of the channel heads
144 ~~and extract their geomorphic parameters. We then calculate the migration rates of the~~
145 ~~drainage divides using the channel head parameters. Moreover, we improve the~~
146 ~~method in Zhou et al (2022a) to adapt it to areas where the elevations of outlets and~~
147 ~~channel heads are different across the drainage divide. We apply these two methods in~~
148 ~~each case to calculate the drainage divide migration rates. This study aims to establish~~
149 ~~an approach to derive the migration rate of drainage divides, at a high precision and~~
150 ~~low cost, based on topographic analysis. Moreover, b~~Combining with enefiting from
151 the ~~geological and low-temperature thermochronology studies of the Wutai Shan~~

152 ~~(Middleton et al., 2017; Clinkscales et al., 2020) detailed tectonic research and the~~
153 ~~high-resolution topographic data on the of Wutai Shan~~, we also attempt to quantify the
154 ~~influence of the~~ cross-divide difference in uplift rates ~~on to improve~~ the precision of
155 drainage-divide migration rate.

156

157 **2. Methods**

158 **2.1 Channel-head-point method**

159 According to the detachment-limited stream power model (Howard and Kerby,
160 1983; Howard, 1994), the channel's erosion rate (E) can be expressed as:

$$161 \quad E = KA^m S^n \quad \text{_____} \quad (1)$$

162 where K is the erosion coefficient, A is the upstream drainage area, S is the gradient of
163 the river channel, and m and n are empirical constants.

164 Because of ~~the threshold mechanisms~~ such as erosion threshold (the shear stress of
165 overland flow must exceed the threshold of the cohesion of bed material to generate
166 river incision) (Howard and Kerby, 1983; Perron et al., 2008) or landslide threshold
167 (landslides occur when the threshold of soil or rock strength is exceeded in high relief
168 region) (Burbank et al., 1996; Tucker et al., 1998), river channels (following Eq. 1)

169 emerge at a certain distance from the drainage divide. The region between the channel
170 head and the drainage divide is referred to as the hillslope area, where the erosion is
171 controlled by landslide, collapse, and diffusion processes (Stoke and Dietrich, 2006;
172 Stark, 2010; Braun et al., 2018; Dahlquist et al., 2018). The channel-head point is the

173 highest and the closest point to the drainage divide on a river channel (Clubb et al.,
174 2014). Therefore, the erosion rate at channel-head points (E_{ch}) can be described as:

$$175 \quad E_{ch} = KA_{cr}^m S_{ch}^n \quad \text{_____} \quad (2)$$

176 where E_{ch} is the erosion rate at channel-head points, A_{cr} is the critical upstream
177 drainage area of a channel-head point (Duvall et al., 2004; Wobus et al., 2006), and
178 S_{ch} is the channel-head gradient measured along the channel at near the channel-head
179 point.

180 ~~To investigate the influence of the key parameters on the channel head erosion rate,~~
181 ~~we plot the curves of the channel head erosion rate against the critical area based on~~
182 ~~Eq. 2 for varying channel head gradient and erosion coefficient (Fig. 1). The plots Eq.~~
183 ~~2 show that the channel head erosion rate (E_{ch}) increases monotonically with the~~
184 ~~critical area (A_{cr}). When the critical area is invariant, the channel head erosion rate~~
185 ~~also increases with the channel head gradient. A large erosion coefficient also creates~~
186 ~~a high channel head erosion rate. The results indicates that the side of a drainage~~
187 ~~divide with a higher A_{cr} or S_{ch} can have a higher erosion rate than the other side, of the~~
188 ~~drainage divide and is more likely to pirate the opposite drainage basin. Besides, a~~
189 ~~high erosion coefficient can amplify the drainage basins' basin's erosion rate.~~

190 ~~The d~~Drainage-divide migration is essentially controlled by the cross-divide
191 difference in erosion rates and topographic slope (Beeson et al., 2017; Dahlquist et al.,
192 2018; Chen et al., 2021; Zhou et al., 2022a; Stokes et al., 2022). Furthermore, the
193 differential uplift should also be considered when using ~~when one uses~~ the cross-
194 divide erosion rates at the channel heads to calculate the erosion difference across the

195 divide, ~~one should also consider the influence of differential uplift rates in these~~
 196 ~~channel heads (Zhou et al., 2022a), especially in the case of tectonic tilting uplift~~
 197 ~~(Zhou et al., 2022a)~~. The drainage-divide migration rate (D_{mr}) can be obtained
 198 according to the cross-divide difference in erosion rate and uplift rate and the slopes
 199 across the divide (Zhou et al., 2022a):

$$D_{mr} = \frac{\Delta E_{ch} - \Delta U_{ch}}{\tan\alpha + \tan\beta} \quad \text{_____} \quad (3)$$

201 where ΔE_{ch} is the difference in erosion rate ~~difference~~ between the two sides
 202 (annotated as α and β) of the drainage divide ($\Delta E_{ch} = E_{ch\alpha} - E_{ch\beta}$), The choice of α or
 203 β is arbitrary, and the positive direction of the migration velocity~~velocity~~rate is
 204 assigned as from the α to the β side whereas the negative is the opposite. ΔU_{ch} is the
 205 cross-divide difference in ~~rock~~ uplift rate ($\Delta U_{ch} = U_{ch\alpha} - U_{ch\beta}$), and $\tan\alpha$ and $\tan\beta$ are
 206 the gradients on ~~both~~ each sides of the drainage divide. ~~Combining Eqs. 2 and 3,~~
 207 Assuming the erosion coefficient (K) is the same on both sides of a drainage divide,
 208 Eqs. 2 and 3~~one can allow us to~~ derive the equation of ~~migration velocity of the~~
 209 drainage divide's migration velocity~~rates~~ according to the parameters at the channel-
 210 head points:

$$D_{mr} = \frac{K[(A_{cr}^m S_{ch}^n)_\alpha - (A_{cr}^m S_{ch}^n)_\beta] - \Delta U_{ch}}{\tan\alpha + \tan\beta} \quad \text{_____} \quad (4)$$

212 ~~The choice of α or β is arbitrary, and the positive direction of the migration~~
 213 ~~velocity is assigned as from the α to β side whereas the negative is the opposite. In~~
 214 ~~this equation, we assume the erosion coefficient is unchanged in the vicinity of a~~
 215 ~~drainage divide.~~ If the exact value of K value is unknown, the drainage divide's
 216 unilateral erosion rate can be used as a substitution:

217

$$D_{mr} = \frac{E_{\alpha} \left[1 - \frac{(A_{cr}^m S_{ch}^n)_{\beta}}{(A_{cr}^m S_{ch}^n)_{\alpha}} \right] - \Delta U_{ch}}{\tan \alpha + \tan \beta} \quad (5)$$

218 or:

219

$$D_{mr} = \frac{E_{\beta} \left[\frac{(A_{cr}^m S_{ch}^n)_{\alpha}}{(A_{cr}^m S_{ch}^n)_{\beta}} - 1 \right] - \Delta U_{ch}}{\tan \alpha + \tan \beta} \quad (6)$$

220

E_{α} and E_{β} are the erosion rates of the α ~~to~~ and the β side of the drainage divide,

221

respectively, which can be derived through ~~the~~ cosmogenic nuclides (^{10}Be)

222

concentration measurements ([Beeson et al., 2017](#); [Godard et al., 2019](#); [Hu et al.,](#)

223

[2021](#)). The regional average erosion rate ($\bar{E} = \frac{E_{\alpha} + E_{\beta}}{2}$) can also be used to calculate

224

the migration rate:

225

$$D_{mr} = \frac{2\bar{E} \left[\frac{(A_{cr}^m S_{ch}^n)_{\alpha} - (A_{cr}^m S_{ch}^n)_{\beta}}{(A_{cr}^m S_{ch}^n)_{\alpha} + (A_{cr}^m S_{ch}^n)_{\beta}} \right] - \Delta U_{ch}}{\tan \alpha + \tan \beta} \quad (7)$$

226

Based on Eqs. 4-7, the migration velocity rate of drainage divides can be estimated

227

using channel-head parameters combined with one of the erosion-related parameters,

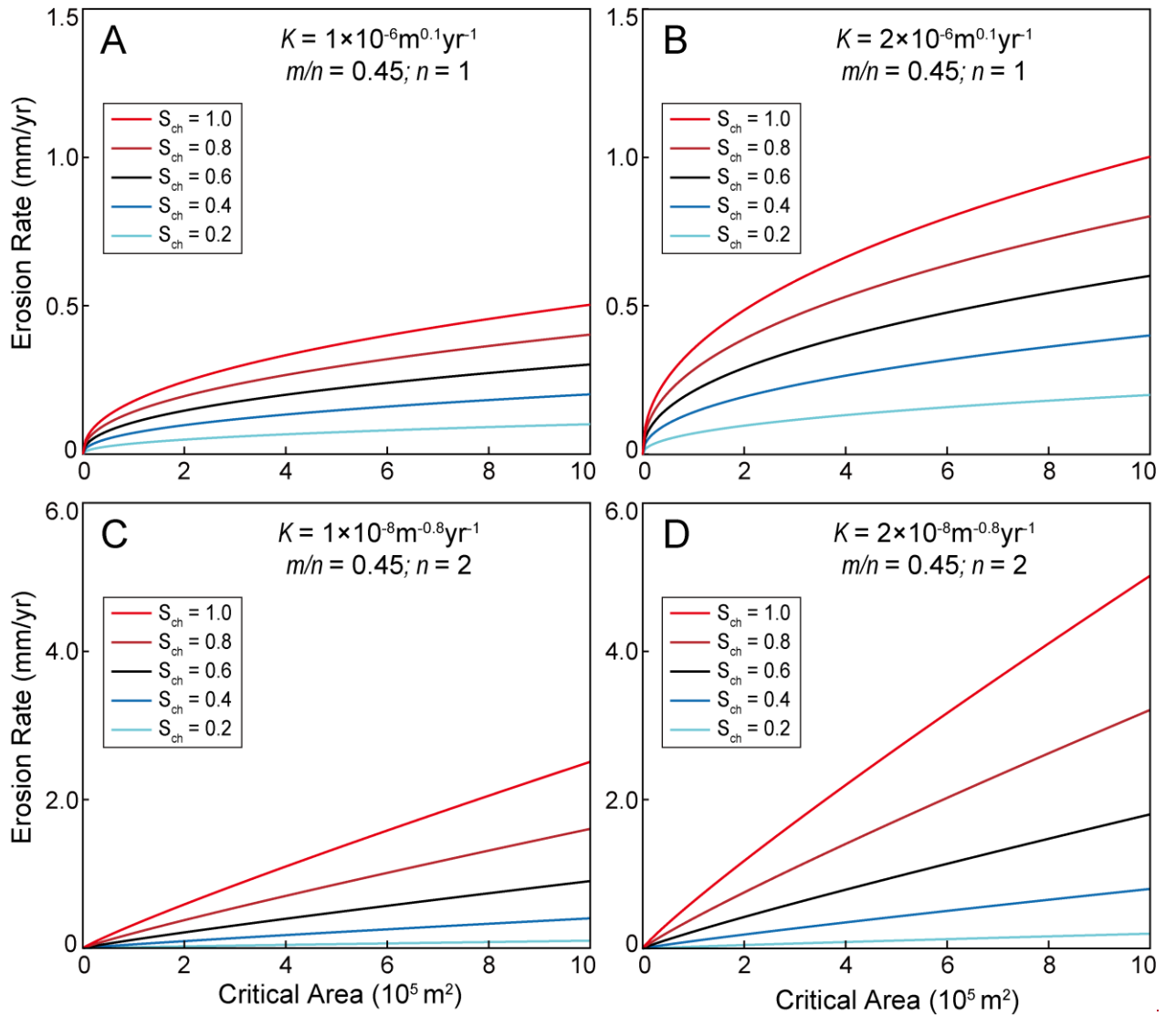
228

~~(~~erosion coefficient (K), erosion rate at one side of a drainage divide (E_{α} or E_{β}), or

229

regional average erosion rate (\bar{E}).

230



231
 232 **Figure 1.** Curves of the channel head erosion rate (E_{ch}) against the critical area (A_{crit})
 233 under different values of channel head gradient (S_{ch}) and erosion coefficient (K). We
 234 assume $m = 0.45$ and $n = 1$ in (A) and (B), and $m = 0.9$ and $n = 2$ in (C) and (D).

235
 236 **2.2 Channel-head-segment method**

237 A Channelchannel-head segment is the channel segment just below the channel-
 238 head (Zhou et al., 2022a). Zhou et al. (2022a) developed a method based on the cross-
 239 divide χ contrast of channel-head segments to calculate the migration velocity-rate of

240 drainage divides. The essence of the method is the cross-divide comparison of the
 241 channel-head segments' [normalized channel](#) steepness (k_{sn}) values. k_{sn} is a widely
 242 used index $(k_{sn} = \frac{E}{K})^{\frac{1}{n}}$ (Whipple et al., 1999; Wobus et al., 2006; Hilley and
 243 Arrowsmith, 2008; Kirby and Whipple, 2012) that is quantitatively related to [erosion](#)
 244 [rate](#) (E) and [erosion coefficient](#) (K) ($k_{sn} = \frac{E}{K})^{\frac{1}{n}}$. χ is an [integral function](#) ($\chi =$
 245 $\int_{x_b}^x \left(\frac{A_0}{A(x)}\right)^{\frac{m}{n}} dx$) of a channels' upstream area (A) to horizontal distance (x) (Royden
 246 et al., 2000; Perron and Royden, 2013), and A_0 is an arbitrary scaling area to make
 247 [the integrand dimensionless](#).

248 [In the research method of Zhou et al. \(2022a\), limited by the resolution of DEM,](#)
 249 [the location of channel heads cannot be accurately identified, because it is limited by](#)
 250 [the resolution of DEM. Therefore, an empirical value of \$A_{cr} = 10^5 \text{ m}^2\$ was used in the](#)
 251 [calculation. Benefiting from the high-resolution DEM in this study, we improve the](#)
 252 [method in Zhou et al. \(2022a\) and use the real location of channel heads to calculate](#)
 253 [the migration rate. Zhou et al. \(2022a\) proposed a cross-divide contrast of \$\chi\$ values, on](#)
 254 [behalf of the inverse of \$k_{sn}\$, which requires the same elevation of the channel heads](#)
 255 [and outlets across the drainage divide. Here, we release this restriction and make this](#)
 256 [method more applicable.](#) When the regional erosion coefficient (K) is known and
 257 unchanged in the vicinity of the drainage divide, the drainage-divide migration rate
 258 can be estimated by the following equation:

$$259 \quad D_{mr} = \frac{K[k_{sn(\alpha)}^n - k_{sn(\beta)}^n] - \Delta U_{ch}}{\tan\alpha + \tan\beta} = \frac{K\left\{\left[\frac{(z_{ch}-z_b)_\alpha}{\chi_\alpha}\right]^n - \left[\frac{(z_{ch}-z_b)_\beta}{\chi_\beta}\right]^n\right\} - \Delta U_{ch}}{\tan\alpha + \tan\beta} \quad (8)$$

260 where z_{ch} and z_b are the elevations of the channel heads and [catchment](#) outlets,
 261 [respectively, and \$\chi\$ is an integral function of channels' upstream area \(\$A\$ \) to horizontal](#)

262 distance (x) (Perron and Royden, 2013; Willet et al., 2014). The detailed derivation of
 263 Eq. 8 is in the Supplementary Materials. The drainage divide's unilateral erosion
 264 rate (E_α or E_β) can also be used as a substitution for the K value:

$$265 \quad D_{mr} = \frac{E_\alpha \left\{ 1 - \left(\frac{\chi_\alpha}{\chi_\beta} \right)^n \left[\frac{(z_{ch}-z_b)_\alpha}{(z_{ch}-z_b)_\beta} \right]^{-n} \right\} - \Delta U_{ch}}{\tan\alpha + \tan\beta} \quad (9)$$

266 or:

$$267 \quad D_{mr} = \frac{E_\beta \left\{ \left(\frac{\chi_\alpha}{\chi_\beta} \right)^{-n} \left[\frac{(z_{ch}-z_b)_\alpha}{(z_{ch}-z_b)_\beta} \right]^n - 1 \right\} - \Delta U_{ch}}{\tan\alpha + \tan\beta} \quad (10)$$

268 Alternatively, one can use the regional average erosion rate (\bar{E}) to calculate the
 269 migration rate:

$$270 \quad D_{mr} = \frac{2\bar{E} \left\{ \frac{\left[\frac{(z_{ch}-z_b)_\alpha}{(z_{ch}-z_b)_\beta} \right]^n - \left(\frac{\chi_\alpha}{\chi_\beta} \right)^n}{\left[\frac{(z_{ch}-z_b)_\alpha}{(z_{ch}-z_b)_\beta} \right]^n + \left(\frac{\chi_\alpha}{\chi_\beta} \right)^n} \right\} - \Delta U_{ch}}{\tan\alpha + \tan\beta} \quad (11)$$

271 Based on Eqs. 8-11, the drainage-divide migration rate can be estimated using the χ
 272 values of high-base-level channel segments combined with one of the erosion-
 273 related parameters (K , erosion coefficient), erosion rate at one side of a drainage
 274 divide (E_α or E_β), or regional average erosion rate (\bar{E}) (erosion coefficient, erosion rate
 275 at one side of a drainage divide, or regional average erosion rate).

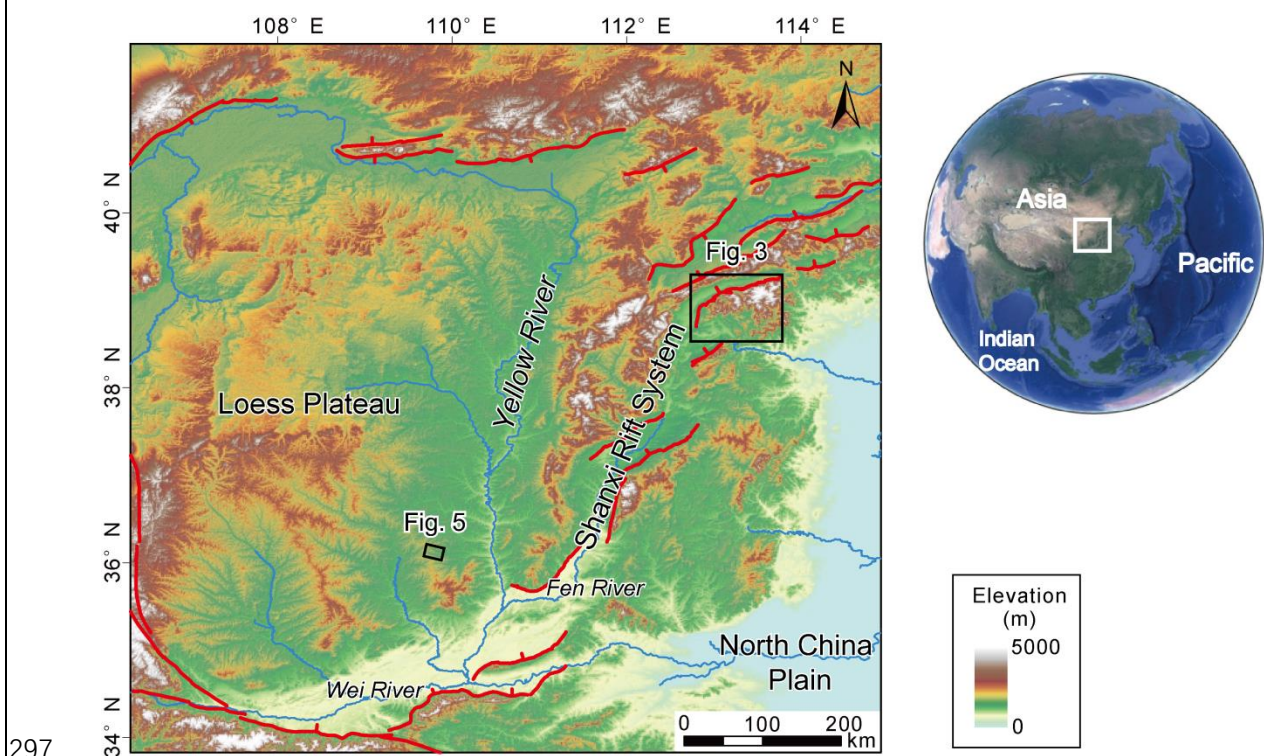
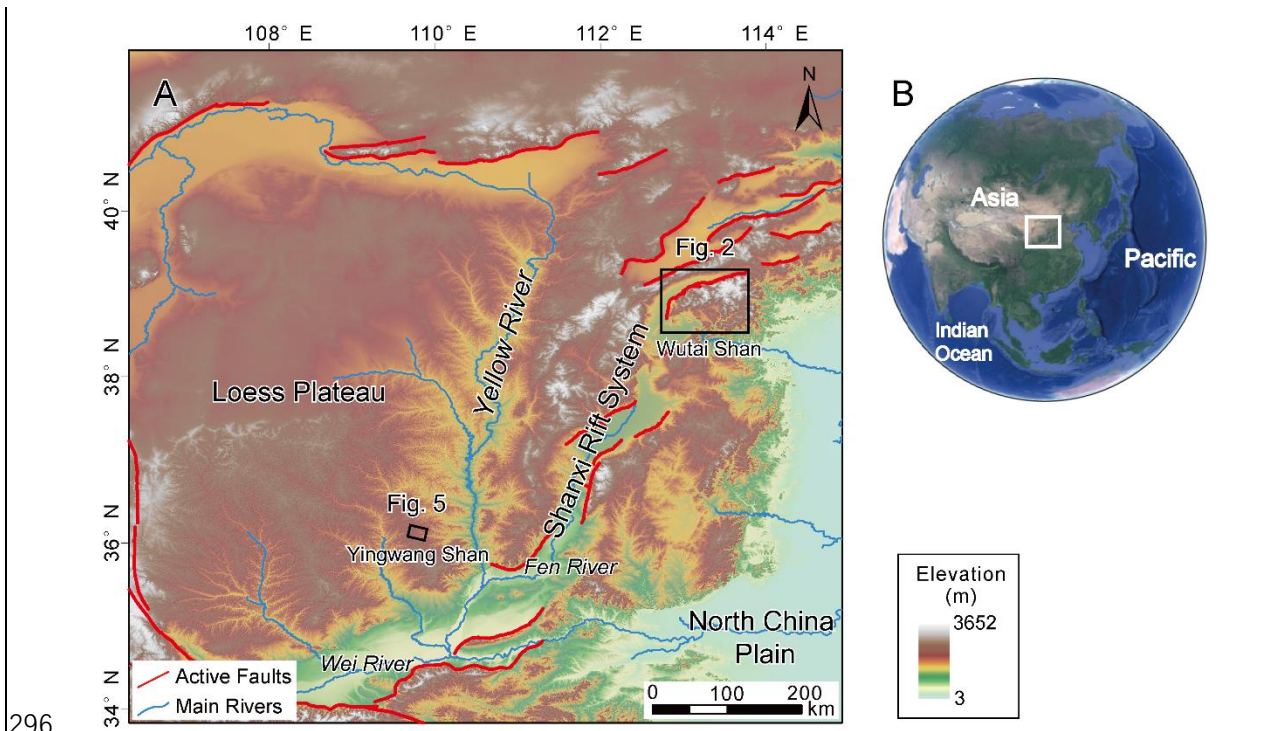
276 We use UAV-acquired aerial photography and structure from motion (SfM)
 277 photogrammetry to derive the high-resolution DEM of the two study areas, the Wutai
 278 Shan in the Shanxi Rift, and the Yingwang Shan in the Loess Plateau, both located in
 279 North China (Fig. 1). The spatial resolution is 0.67 m in the Wutai Shan, and 0.84 m
 280 spatial resolution in the Wutai Shan and in the Yingwang Shan respectively). Based
 281 on the high-resolution topography data, we extract the relevant parameters and

282 calculate the drainage-divide migration rate using the two methods above for each
283 case. Analysis of the data is based on the Matlab toolbox TAK (Forte and Whipple,
284 2019) and TopoToolbox (Schwanghart and Scherler, 2014).

285

286 **3. Applications to natural cases**

287 We apply the new methods to two natural examples in North China, the Wutai
288 Shan, in the Shanxi Rift and the Yingwang Shan in the Loess Plateau~~Loess Plateau~~
289 ~~(Fig. 12)~~, to demonstrate how to calculate the drainage-divide migration rates (Fig. 1).
290 ~~We use UAV-acquired aerial photography and structure from motion (SfM)~~
291 ~~photogrammetry to derive the sub-meter digital elevation model of the two study~~
292 ~~areas. Based on the high-resolution topography data (sub-meter), we extract the~~
293 ~~relevant parameters and calculate the drainage-divide migration rate using the two~~
294 ~~methods above for each case. Analysis of the data is based on the Matlab toolbox~~
295 ~~TAK (Forte and Whipple, 2019) and TopoToolbox (Schwanghart and Scherler, 2014).~~



298 **Figure 12.** Locations and tectonic background of the two nature cases in North China.

299 The figure is modified according to the from Fig. 7 in Shi et al. (2021). (A) Red
 300 curves-lines represent the main active faults. Black rectangles show the locations of
 301 the two nature cases. Red curve denotes active fault, The fault data is downloaded

302 ~~sourced from the site~~ (<https://www.activefault-datacenter.cn/>). The topography data
303 ([ALOS DEM, 12.5 m resolution](#)) is downloaded from the Alaska Satellite Facility
304 ([ASF](#)) Data Search (<https://search.asf.alaska.edu/>). (B) The satellite image is
305 downloaded from Google Earth. ~~White rectangles show the location of p~~Panel A. ~~The~~
306 ~~satellite image is downloaded from Google Earth.~~

307

308 3.1 Wutai Shan

309 The Wutai Shan is a tilted fault block on the shoulder of the Shanxi Rift System
310 located in the central North China craton ([Fig. 1A](#)) (Xu et al., 1993; Su et al., 2021).
311 The tilting uplift of the Wutai Shan is controlled by the Northern Wutai Shan fault
312 ([Fig. 3A](#)), and there is no active fault along the south edge of the Wutai Shan horst
313 ([Fig. 2A](#)). The bedrock of the Wutai Shan area ~~consists mainly of~~ ~~is mainly~~
314 metamorphic and igneous basement rocks (Clinkscales et al., 2020; ~~Zhou et al 2022a~~)
315 and there is no obvious variation in rock erodibility and precipitation in this area ([Fig.](#)
316 [S2 & S3](#)). ~~Zhou et al. (2022b) reveals that the Wutai Shan drainage divide is~~
317 ~~migrating northwestward due to the tilting uplift and predicts the drainage divide will~~
318 ~~move ~10 km to the northwest to achieve a steady state if all geological conditions~~
319 ~~remain. Morphological-Geomorphic evidence also shows exhibits a clear~~
320 ~~northwestward migration of the drainage divides (Fig. 3). Figure 3~~The plan and
321 ~~satellite views shows several barbed tributaries and a captured area in~~around the
322 ~~Wutai Shan drainage divide, which indicate that the tributaries formerly part of the~~

323 northern drainage have become part of the southern drainage (Fig. 3A&B),
324 where there are clear barbed tributaries and a capture point. The χ -plots analysis
325 shows the southern side of the drainage divide has steeper channels, higher k_{sn} , and
326 lower χ . The χ -plots of paired rivers show illustrate obvious characteristics of
327 aggressorshrinkingshrinking-expandingvictim and captured-beheaded rivers (Fig. 3C).

328

329 To derive the erosion coefficient of the Wutai Shan area, we calculate the

330 channel steepness (k_{sn}) values of this region, under the assumption of assuming $n = 1$
331 and $m = 0.45$ (Wobus et al., 2006; DiBiase et al., 2010; Perron and Royden, 2012;
332 Wang et al., 2021). We then and use the Kriging interpolation technique method to
333 generate the k_{sn} distribution map (Fig. 23B). In addition, The results of under the
334 assumptions of $m = 0.35$ and 0.55 , respectively, are shown in the sSupplementary
335 mMaterials (Fig. S4). The average k_{sn} value of the upthrown side near the Northern
336 Wutai Shan fault of this area is $\sim 80 \text{ m}^{0.9}$ (Fig. 23D). The Previous geological study
337 shows that the Quaternary throw rates of the Northern Wutai Shan fault are 0.8-1.6
338 mm/a (Middleton et al., 2017). The According to a low-temperature thermochronology
339 study shows that the time-averaged long-term throw rates in the late Cenozoic of the
340 Wutai Shan (Clinkscales et al., 2020), the erosion rate of the sampling area (in the
341 footwall block of the northern boundary fault of the Wutai Shan) is about 0.25 mm/yr,
342 and there is an accelerated activity in the Wutai Shan area in the late
343 Cenozoic(Clinkscales et al., 2020). According to the above geological and low-
344 temperature thermochronology these studies, we assume a $0.50 \pm 0.25 \text{ mm/yr}$

345 uplift/erosion rate in the northern margin of the Wutai Shan (at in the footwall of the
346 Northern Wutai Shan fault). The average k_{sn} value of this area is $\sim 80 \text{ m}^{0.9}$ (Fig. 3).
347 According to Combining with the equation, $K = \frac{E}{k_{sn} n}$, and following the approach of
348 previous studies (Kirby and Whipple, 2001; Kirkpatrick et al., 2020; Ma et al., 2020),
349 the erosion coefficient (K) is calculated to be $(6.25 \pm 3.13) \times 10^{-6} \text{ m}^{0.1} \text{ yr}^{-1}$ in the
350 Wutai Shan area. Because there is no obvious variation in rock erodibility and
351 precipitation in this area (Fig. S2 & S3), we use this value as the erosion coefficient
352 (K) of the Wutai Shan area.

353
354 We then apply the two above new methods in this area to calculate the migration
355 velocity rate of the drainage divide in the Wutai Shan. We first randomly choose three
356 pairs of rivers (Fig. 4A) and make acquire their slope-area plots (Figs. 4B, E, H) and
357 the χ -plots (Figs. 4C, F, I). According to the location of the river's scatchment outlets
358 (Fig. 4A), we obtain the river's outlet elevations (z_b) from the river's long profiles.
359 According to the breaking point of the slope-area regression line plot (Duvall et al.,
360 2004) (Figs. 4B, E, H), we obtain the values of the critical upstream drainage area
361 (A_{cr}). According to these values, and its corresponding position on the χ plot, we can
362 separate hillslope and channel areas and mark the position of the channel heads on the
363 χ -plots and the topography map (Fig. 4A). For the slope-area plots, we derive the
364 value of critical upstream drainage area (A_{cr}) according to the position of the channel
365 heads. The $\tan\alpha$ and $\tan\beta$ are in line with the gradient of channel head points (S_{ch}) on
366 each side of the drainage divide (Figs. 4D, G, J). Because the slopes of the channel-

367 ~~head points varies, we use the average slope of the hillslope area as the value of~~
368 ~~channel head gradient (S_{ch}). Moreover, for the χ -plots (Figs. 4C, F, I), we obtain the~~
369 ~~elevations of outlets (z_b) and channel heads (z_{ch}) of the channel segment, and the χ~~
370 ~~values according to based on the position coordinate of the channel-head points.~~
371 According to the location of the channel heads on the river's long profiles, we
372 calculate the slope of the channel heads' tangent lines, and derive the channel-head
373 gradient (S_{ch}). The Topographic gradient ($\tan\alpha$ or $\tan\beta$) is calculated through the
374 average slope of the hillslope segment near the channel head (Stokes et al., 2022) (not
375 including the hilltop part).

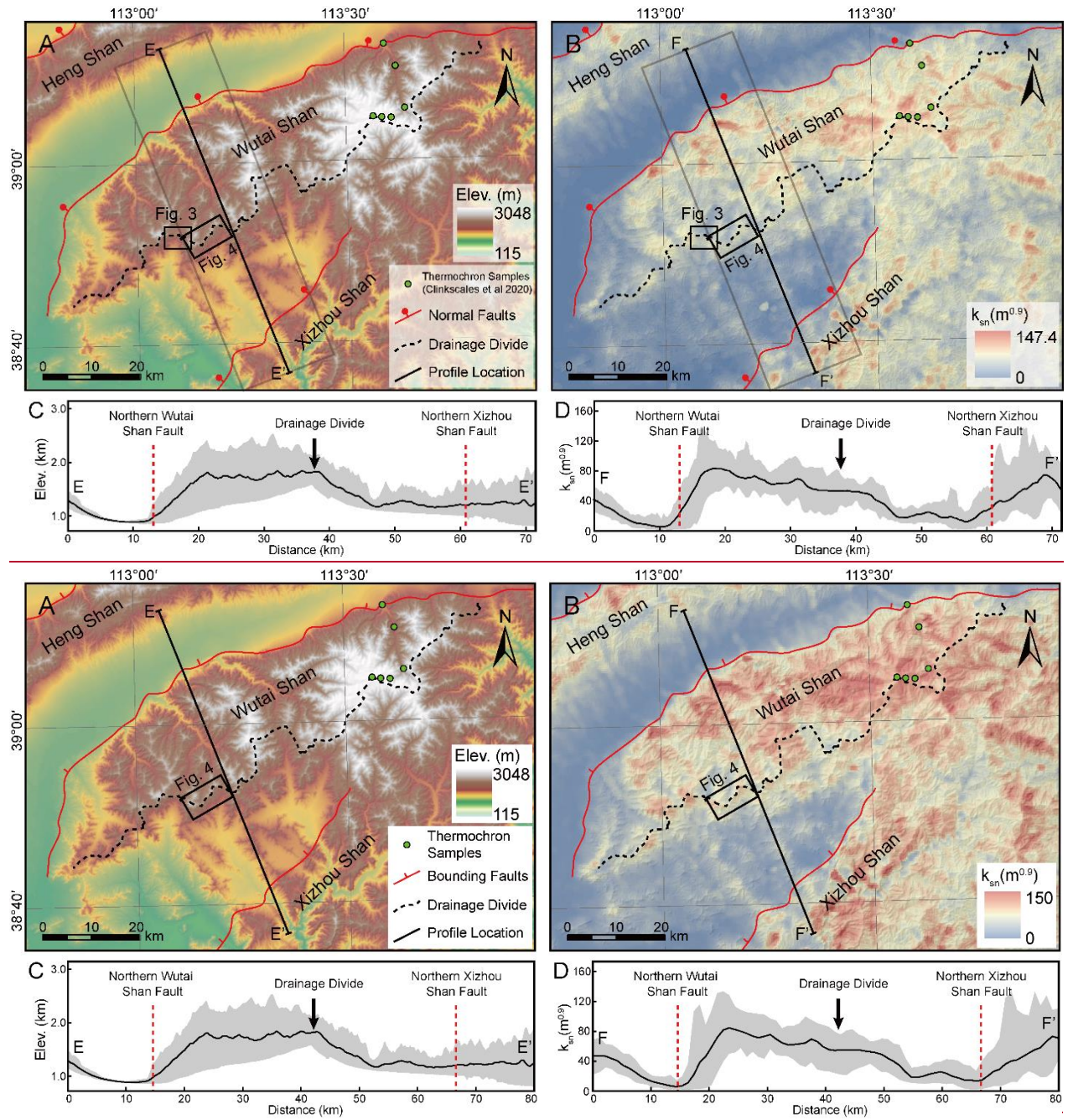
376 If we assume the rock uplift rate decreases linearly from 0.25 to 0 mm/yr from
377 northwest to southeast of the Wutai Shan horst (~40 km wide), the cross-divide uplift
378 difference in the channel-head points (ΔU_{ch}) (the distance perpendicular to the along
379 the normal direction of the boundary fault is ~600 m) is ~0.0084 mm/yr. ~~The $\tan\alpha$ and~~
380 ~~$\tan\beta$ are in line with the gradient of channel head points (S_{ch}) on each side of the~~
381 ~~drainage divide (Figs. 4D, G, J). We assume $n = 1$ and $m = 0.45$ in the calculation~~
382 ~~following previous studies (Wobus et al., 2006; DiBiase et al., 2010; Perron and~~
383 ~~Royden, 2013; Wang et al., 2021).~~ After determining these parameters, we adopt the
384 channel-head-point (Eq. 4) and channel-head-segment (Eq. 8) methods, respectively,
385 to calculate the migration rates. The required data for calculation and the migration
386 rates are shown in Table 1. The calculated results of for $m = 0.35$ and 0.55 ,
387 respectively, are shown in the sSupplementary mMaterials (Table S1).

388 The rivers have different characteristics on both sides of the drainage divide,

389 ~~according to as illustrated on their~~Both the slope-area plots (Figs. 4B, E, H) and the χ -
390 plots (Figs. 4C, F, I). ~~show that distinct character of the rivers across the drainage~~
391 ~~divide.~~For the first site (Fig. 4D), the migration rates calculated by ~~both~~ the channel-
392 head-point and channel-head-segment methods are 0.~~12-21~~ mm/yr (~~northward~~) and
393 0.26 mm/yr (northwestward), respectively. For the second site (Fig. 4G), the
394 migration rates ~~derived from the two methods~~ are 0.~~11-23~~ mm/yr (~~northward~~) and
395 0.13-27 mm/yr (northwestward), respectively. For the third site (Fig. 4J), ~~the~~
396 ~~migration rates are~~ 0.~~12-21~~ mm/yr (~~northward~~) and 0.~~10-22~~ mm/yr (~~northwestward~~),
397 respectively. The drainage divides of all three points are ~~predicted to migrate~~
398 migrating northwestward, which is consistent with ~~the~~ previous result inferred by the
399 cross-divide contrast of slopes in this area (Zhou et al., 2022b). ~~Furthermore, the~~
400 migration ~~velocities-rates~~ calculated by the two methods are comparable in all three
401 sites. Morphological evidence also shows a clear northward migration of the drainage
402 divides (Fig. 3). Figure 3 shows a captured area in the Wutai Shan, where there are
403 clear barbed tributaries and a capture point. The south side of the drainage divide has
404 steeper channels, higher k_{sn} , and lower χ . The χ plots of rivers show obvious
405 characteristics of aggressor victim and captured beheaded rivers (Fig. 3).

406

407



408

409

410 **Figure 23. (A-&B)-Topography (A) and normalized channel steepness (k_{sn}) (B)**
 411 **distribution of the Wutai Shan horst and surrounding area in the Shanxi Rift System.**

412 The black dashed **curve-line** shows the location of the main drainage divide. Red

413 **curves-lines** show the main **bounding-active** faults. The black **straight**-lines show the

414 location of **the**-profiles E-E' and F-F'. Black rectangles show the area of **aerial**

415 **photography** (Fig. 3B & 4A). **Gray rectangles-boxes** show the area of the **swath**

416 profiles in Panels C& and D. Green dots denote the locations of the low-temperature
417 thermochronology samples in Clinkscales et al. (2020). The topography data (ALOS
418 DEM, 12.5 m resolution) is downloaded from the Alaska Satellite Facility (ASF) Data
419 Search (<https://search.asf.alaska.edu/>). The k_{sn} is calculated using TopoToolbox
420 (Schwanghart and Scherler, 2014)~~based on Matlab~~, and the interpolation uses the
421 Kriging method on ArcGIS. (C) ~~The~~ Topography swath profile along E-E'. See
422 location in Fig. 3 Panel A. (D) ~~The~~ k_{sn} swath profile along F-F'. See location in Fig.
423 3 Panel B. The swath profiles are extracted using TopoToolbox (Schwanghart and
424 Scherler, 2014). The red ~~dotted-dashed~~ lines shows the location of the main ~~bounding~~
425 active normal faults, and the black arrow shows the location of the main drainage
426 divide. Both swath profiles are 20 km wide (10 km on each side). The extent of the
427 swath profiles is represented by the grey boxes in Panel A&B.
428

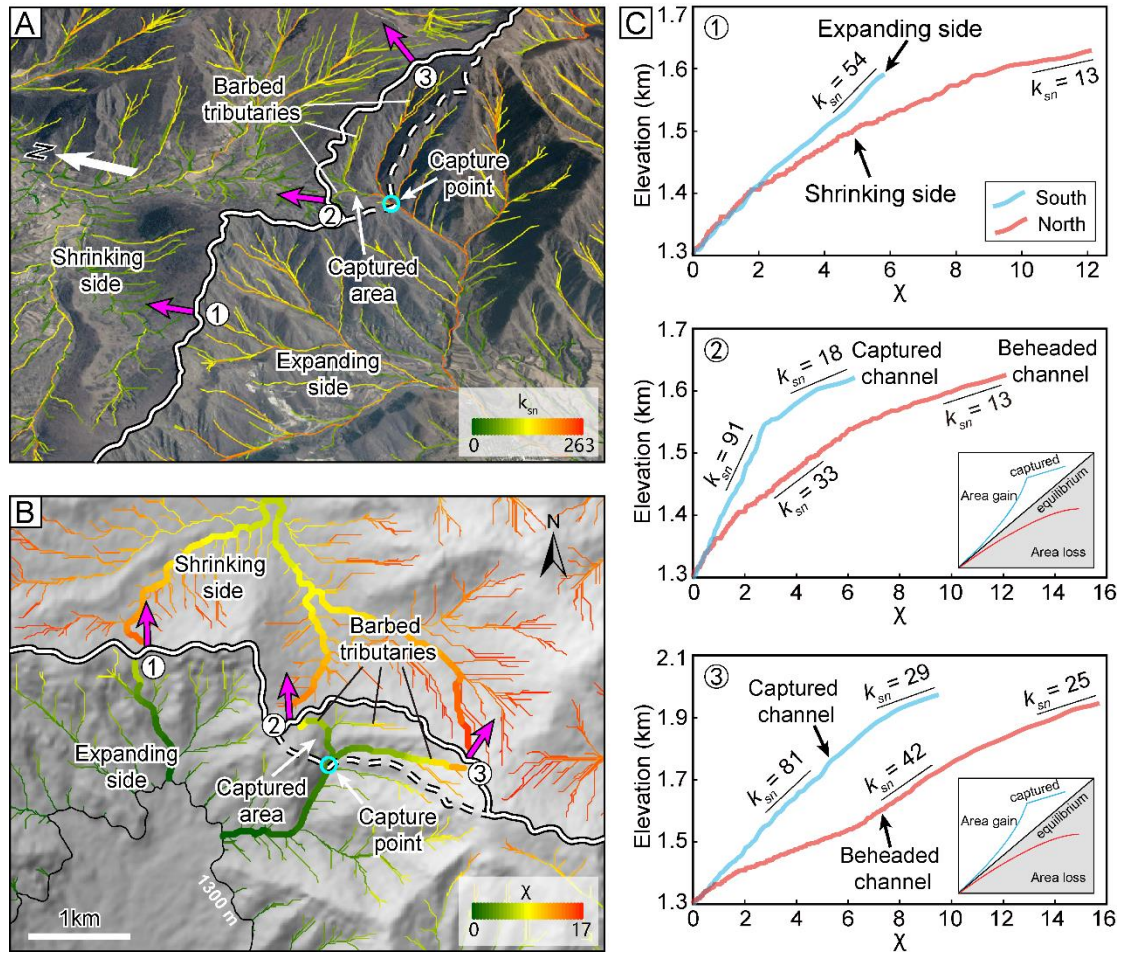


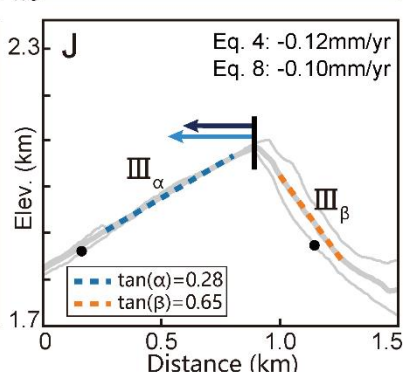
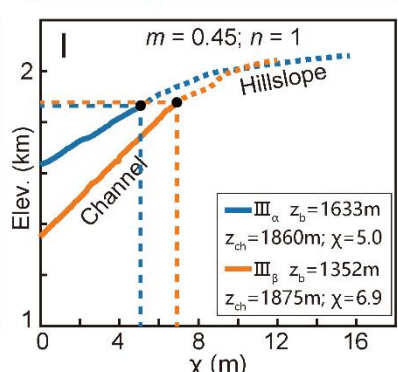
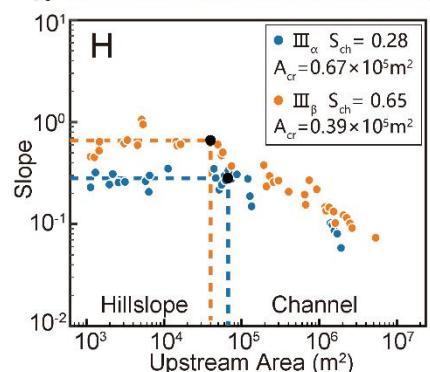
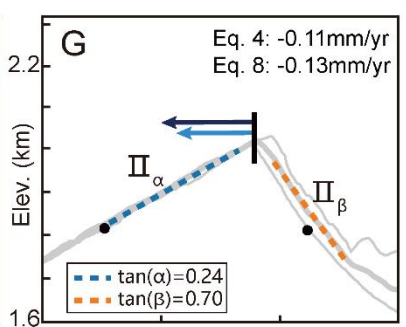
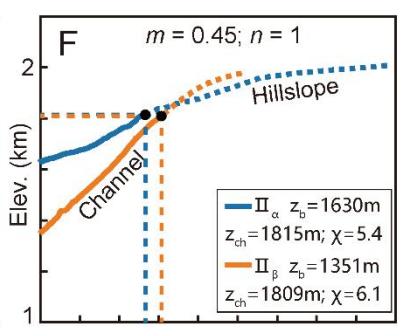
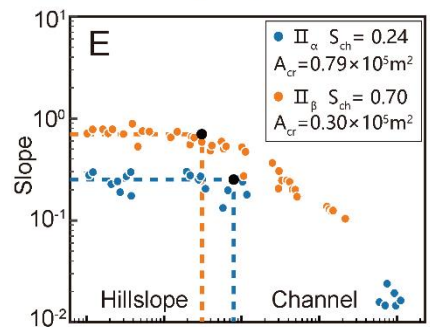
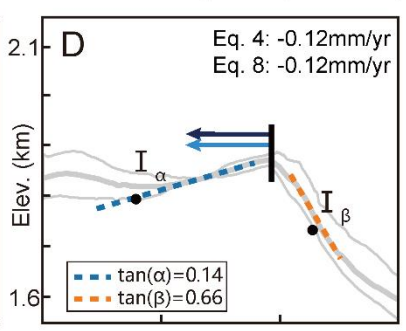
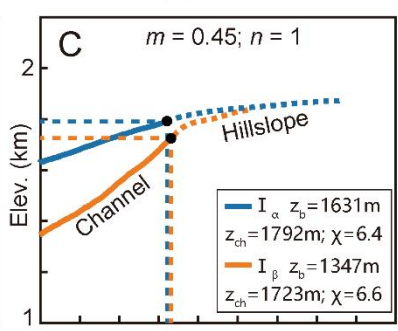
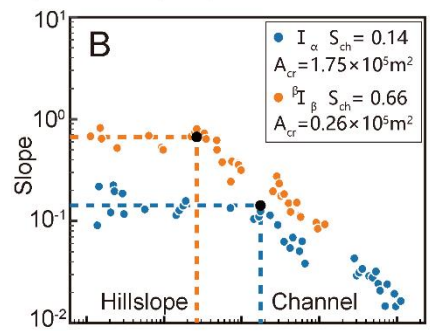
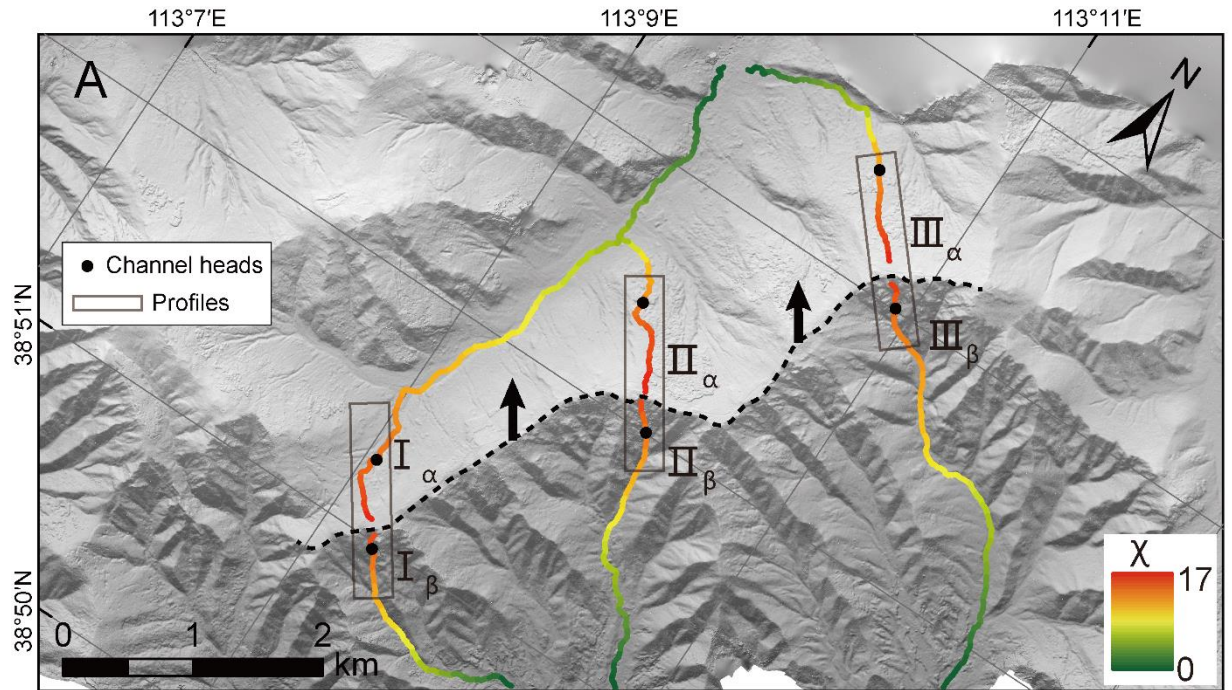
Figure 3. Perspective views and χ map of the drainage divide in the Wutai Shan

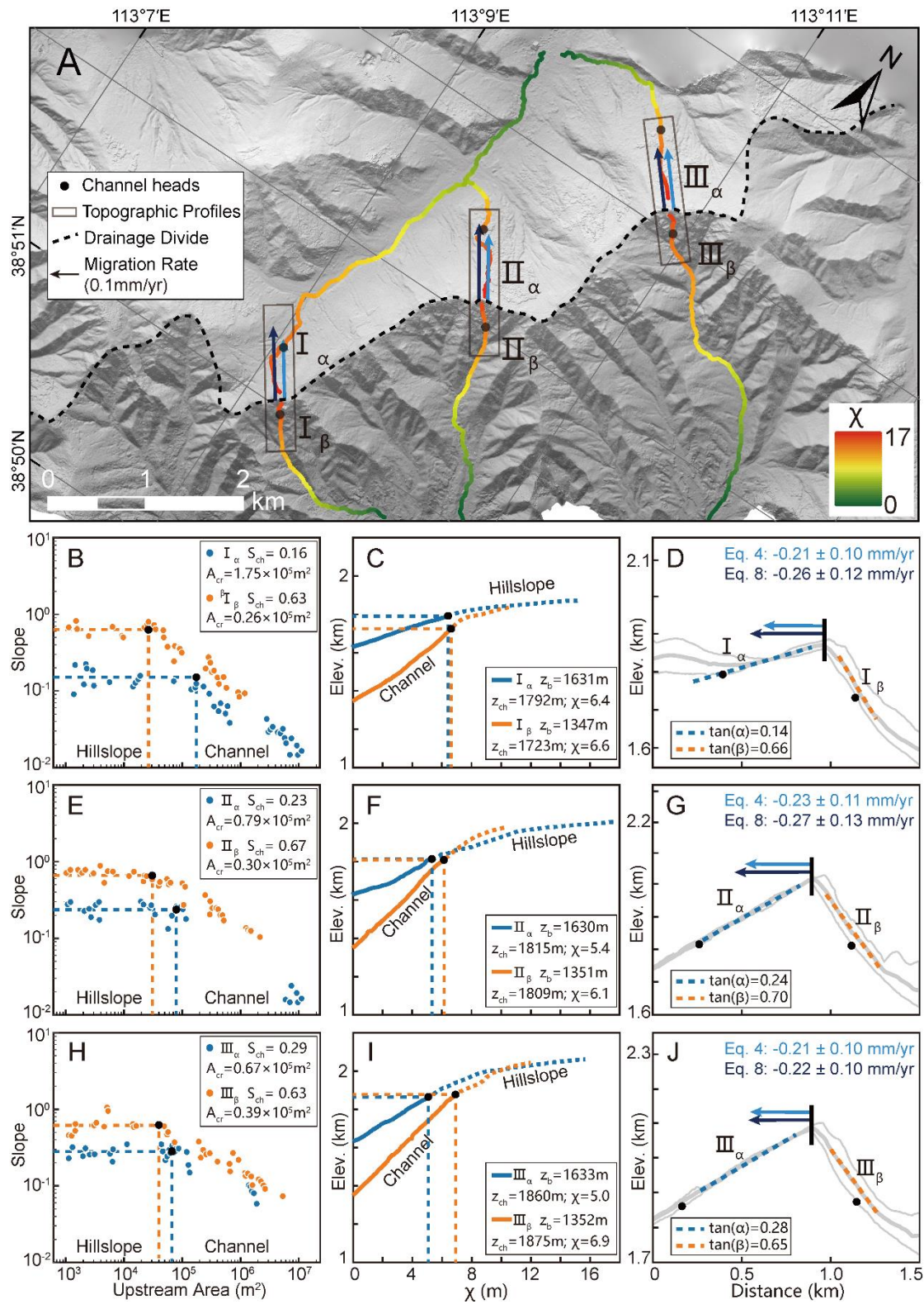
(The location is shown in see Fig. 2 for location). (A) Perspective views of the captured area and the channels mapped with k_{sn} . The south side of the drainage divide has steeper channels and higher k_{sn} than the north side. Red-Magenta arrows show drainage divide migration directions. The satellite image is downloaded from Google Earth. (B) The χ map of this area with the outlet elevation of 1300 m. The south side of the drainage divide has lower χ values than the north side. It should be noted that the catchment outlet at the north side of the drainage basins (the 1300 m contour) is out of the map. The χ -plots of the rivers in bold lines are shown in Panel C. The topography data (ALOS DEM, 12.5 m resolution) is downloaded from the Alaska

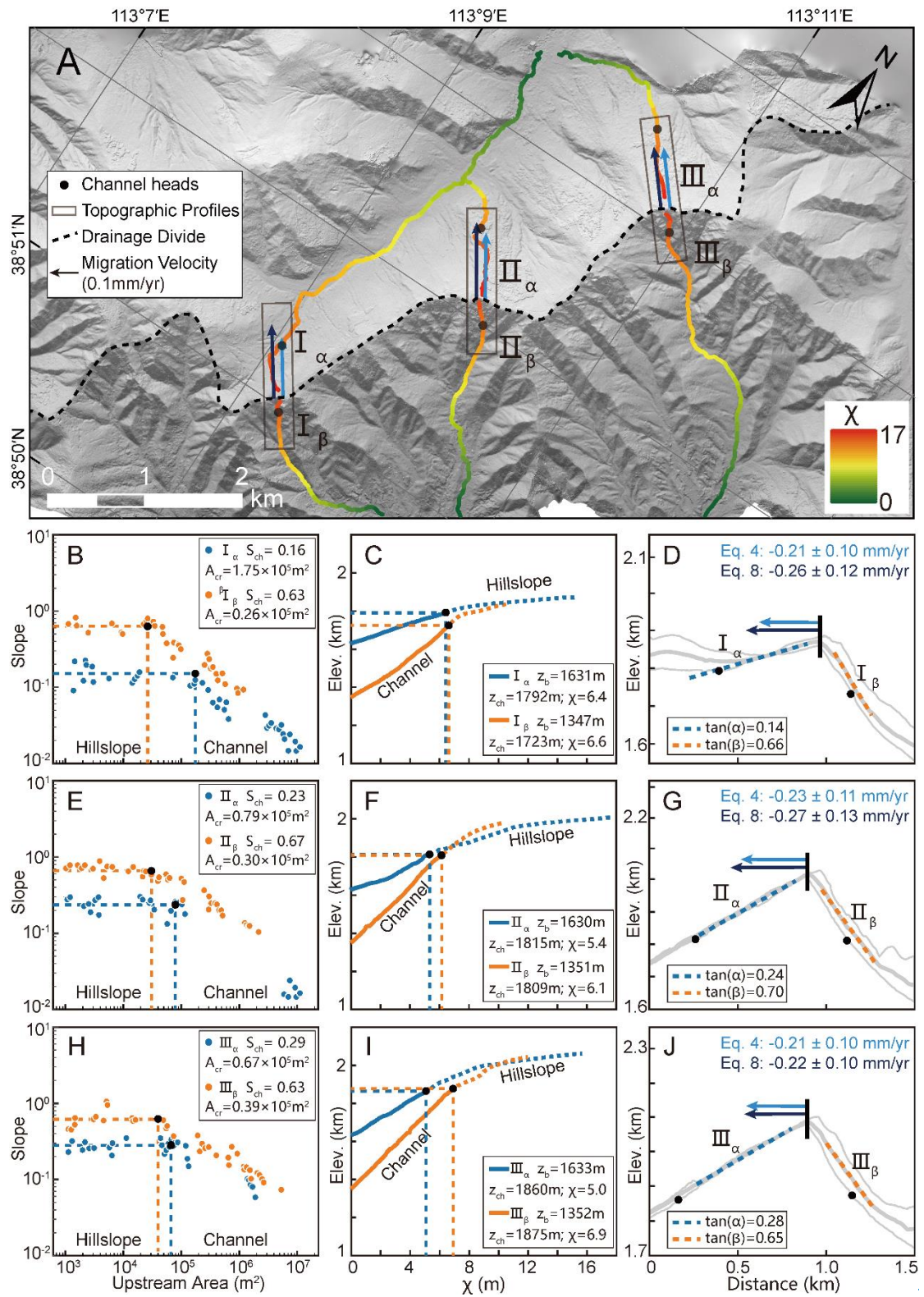
440 Satellite Facility (ASF) Data Search (<https://search.asf.alaska.edu/>). (C) χ -plots of the
441 three paired rivers in Panel B. The blue and red curves correspond to the rivers
442 on the south and north sides, respectively. The χ -plot of River 1 is steeper on the south
443 side, indicating that the river on the south side is the aggressor expanding and is the
444 victim the river on the north side is shrinking. The χ -plots of Rivers 2& and 3 in the
445 captured area show obvious characteristics of the captured and beheaded rivers. The
446 χ -plot is extracted using TAK (Forte and Whipple, 2019) and TopoToolbox
447 (Schwanghart and Scherler, 2014).

448

449







452

453 **Figure 4.** Analytical results of the Wutai Shan drainage divide. (A) High-resolution

454 hill-shade topographic map (0.67 sub-meter spatial resolution) of the Wutai Shan. The

455 black dashed curve line shows the location of the main drainage divide. Colored

456 curvelines show the three pairs of selected channels used for analysis. The black dots
457 are the channel heads. Black rectangles show the location of the cross-divide
458 topography swath profiles. The black arrows show the direction of drainage-divide
459 migration (**B, E, H**) Slope-area plots of the three pairs of selected channels. The blue
460 and orange dots are the slope-area plots of the north (α) and south (β) sides of the
461 drainage divide respectively. The black dots represent the channel heads. (**C, F, I**) χ -
462 plots of the selected channels. The blue and orange curvelines are the χ -plots of the
463 north (α) and south (β) sides of the drainage divide respectively. The black dots
464 represent the channel heads. (**D, G, J**) Cross-divide topography swath profiles with
465 the drainage-divide migration rates. The locations of the profiles are in Fig. 4pPanel
466 A. The light and dark blue arrows are the drainage-divide migration rates calculated
467 by the channel-head-point (Eq. 4) and channel-head-segment (Eq. 8) methods
468 respectively.

469

470 **3.2 An unnamed mountain range in the Loess Plateau Yingwang Shan**

471 The Loess Plateau is hosted by the tectonically stable Ordos Block of the North
472 China craton (Yin, 2010; Su et al., 2021). Over the past 2.6 million years, it has
473 accumulates-accumulated tens to hundreds of meters of eolian sediments over the past
474 2.6 million years (Yan et al., 2014), draping preexisting topography (Xiong et al.,
475 2014). There is no active fault within the study area. The lithology of the study site is
476 mainly loess; thereand is little to no variation in rock erodibility and precipitation

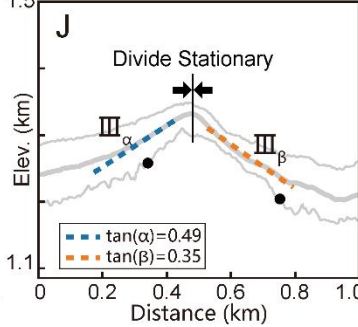
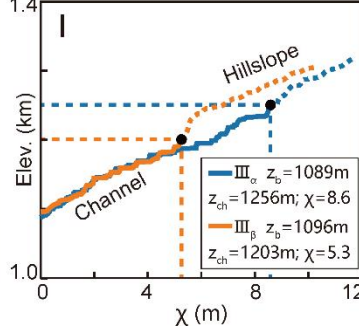
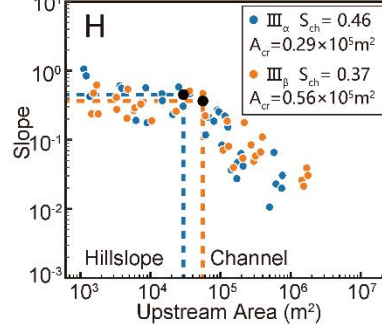
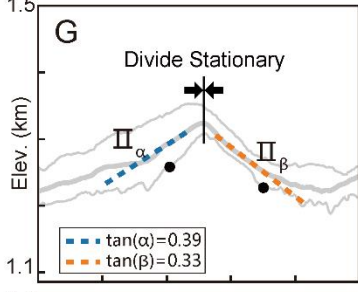
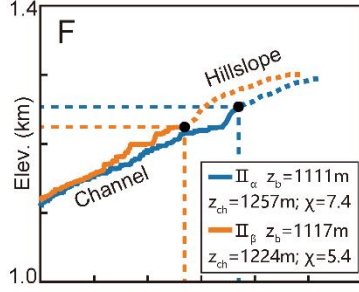
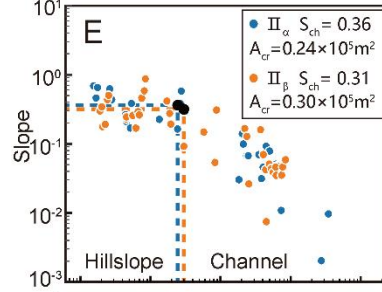
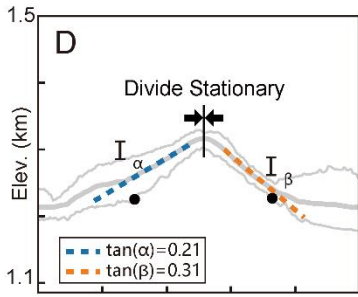
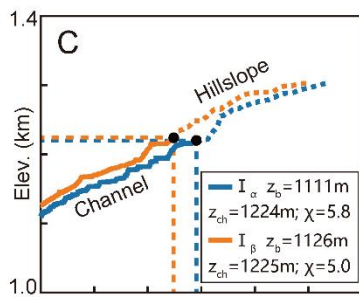
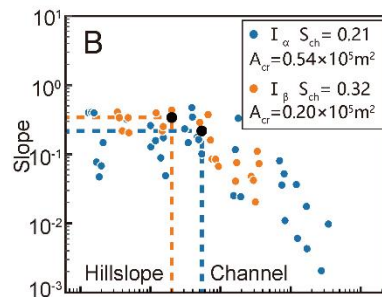
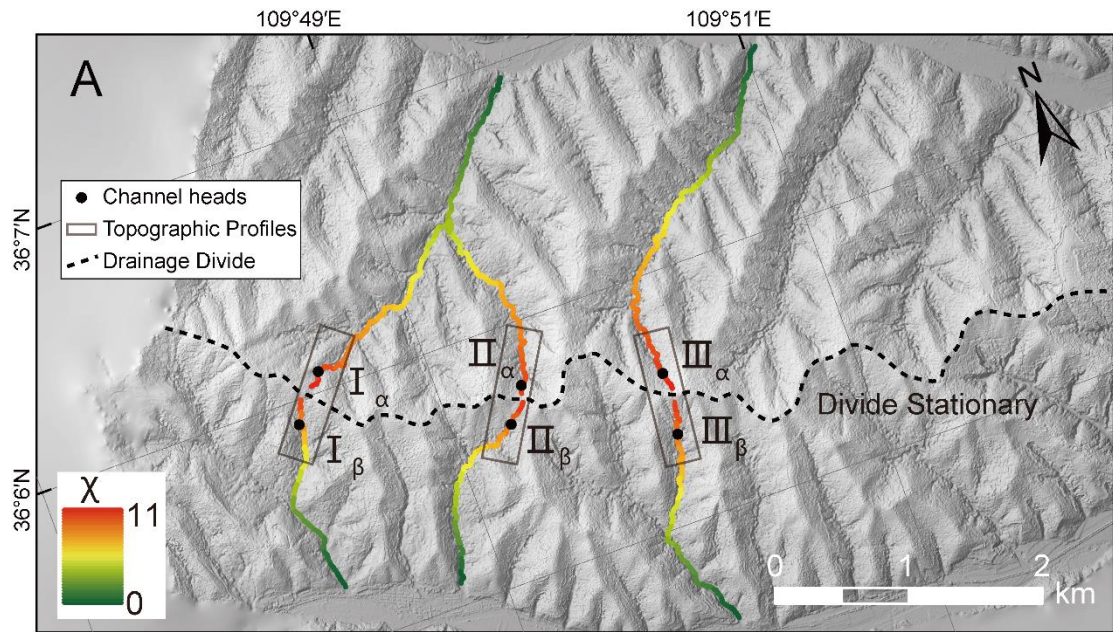
477 within the area (Shi et al., 2020; Zhou et al., 2022b).

478 We apply the two methods ~~in this area to Yingwang Shan of Loess Plateau to~~
479 calculate the drainage-divide migration rate. Similar to the Wutai Shan ~~easesite~~, we
480 ~~first make obtain the randomly choose three pairs of rivers and make their~~ slope-area
481 plots (Figs. 5 B, E, H) ~~and~~ the χ -plots (Figs. 5 C, F, I), ~~and extract the. Then we mark~~
482 ~~the position of the channel head points on the topography map (Fig. 5A), slope-area~~
483 ~~plots, and χ plots. According to its position, we derive the A_{er} -values of A_{cr} , S_{ch} , z_b , z_{ch} ,~~
484 ~~χ , $\tan\alpha$ and $\tan\beta$ of the rivers. from the slope-area plots (Figs. 5 B, E, H) and the χ~~
485 ~~values and the elevations of channel head segments' outlets (z_b) and heads (z_{ch}) from~~
486 ~~the χ plots (Figs. 5 C, F, I). We also acquire the average slope of the hillslope area and~~
487 ~~derive the S_{ch} , $\tan\alpha$, and $\tan\beta$ values.~~

488 The rate of soil erosion in the study area is about $500 \text{ t}\cdot\text{km}^{-2}\cdot\text{yr}^{-1}$ ~~according to the~~
489 ~~distribution of silt discharge (Fu, 1989). If we~~Combining with the ~~assumptione~~ of the
490 density of ~~L~~loess, ~~is~~ $1.65 \text{ t}\cdot\text{m}^{-3}$, the ~~present-day average~~ erosion rate ~~here-in the study~~
491 ~~area~~ is ~~about~~ ~~calculated to be~~ $0.3 \text{ mm}\cdot\text{yr}^{-1}$. Because there is no obvious unequal uplift
492 in this region, we ~~assume~~ ~~assign~~ that ΔU_{ch} is zero. We also assume $n = 1$ and $m = 0.45$
493 in the calculation (~~Wobus et al., 2006; DiBiase et al., 2010; Perron and Royden, 2012;~~
494 ~~Wang et al., 2021~~). Then, we use the methods of channel-head parameters (Eq. 7) and
495 channel segments (Eq. 11) to calculate the drainage-divide migration rates. The
496 required data for calculation and the migration rates are shown in Table 1.

497 All results of the three points show that the drainage-divide migration rate here is
498 close to zero, no matter which method is used in the calculation. The results show that

499 the drainage divide of the study site is in topographical equilibrium, which is
500 consistent with the inference in previous studies ([Willett et al., 2014](#), [Zhou et al.,
501 2022b](#)).
502



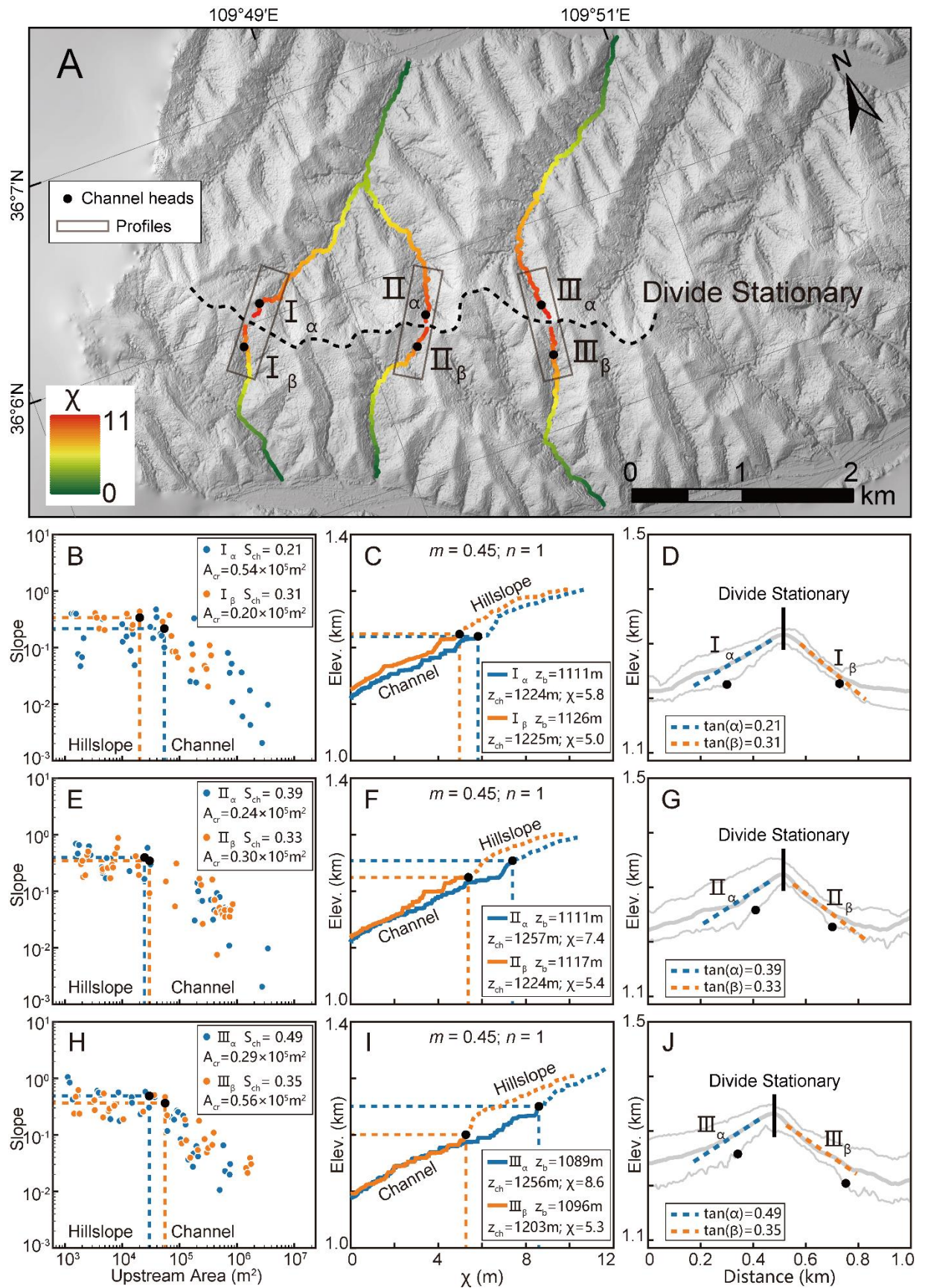


Figure 5. Analytical results of the Yingwang Shan a mountain range in the Loess

506 Plateau. (A) High-resolution hill-shadetopographic map (~~sub-meter~~0.84 m spatial
507 resolution). The black dotted curveline shows the location of the main drainage
508 divide. Colored curvelines show the three pairs of selected channels used for analysis.
509 The black dots represent the channel heads. Black rectangles show the location of the
510 cross-divide topography swath profiles. (B, E, H) Slope-area plots of the three pairs
511 of selected channels. The blue and orange dots are the data of the north (α) and south
512 (β) sides of the drainage divide respectively. The black dots represent the channel
513 heads. (C, F, I) χ -plots of the selected channels. The blue and orange curvelines are
514 the χ -plots of the north (α) and south (β) sides of the drainage divide respectively. The
515 black dots represent the channel heads. (D, G, J) The cross-divide topography swath
516 profiles. The locations of the swath profiles are in Panel A.
517

Table 1. Channel's parameters and the migration rates of the drainage divides ~~in~~ of the two ~~field~~ natural cases.

<u>Natural Cases</u>	<u>No.</u>	<u>A_{cr}</u> ($\times 10^5 \text{m}^2$)	<u>S_{ch}</u>	<u>z_b</u> (m)	<u>z_{ch}</u> (m)	<u>χ</u>	<u>$\tan\alpha$</u>	<u>$\tan\beta$</u>	<u>ΔU_{ch}</u> (mm/yr)	<u>D_{mr} (mm/yr)</u> (Channel-head-point method)	<u>D_{mr} (mm/yr)</u> (Channel-head-segment method)
<u>Wutai Shan</u>	<u>Fig. 4 I_a</u>	<u>1.75</u>	<u>0.16</u>	<u>1631</u>	<u>1792</u>	<u>6.4</u>					
	<u>Fig. 4 I_b</u>	<u>0.26</u>	<u>0.63</u>	<u>1347</u>	<u>1723</u>	<u>6.6</u>	<u>0.14</u>	<u>0.66</u>	<u>~ 0.008</u>	<u>-0.21 ± 0.10</u>	<u>-0.26 ± 0.12</u>
	<u>Fig. 4 II_a</u>	<u>0.79</u>	<u>0.23</u>	<u>1630</u>	<u>1815</u>	<u>5.4</u>					
	<u>Fig. 4 II_b</u>	<u>0.30</u>	<u>0.67</u>	<u>1351</u>	<u>1809</u>	<u>6.1</u>	<u>0.24</u>	<u>0.70</u>	<u>~ 0.008</u>	<u>-0.23 ± 0.11</u>	<u>-0.27 ± 0.13</u>
	<u>Fig. 4 III_a</u>	<u>0.67</u>	<u>0.29</u>	<u>1633</u>	<u>1860</u>	<u>5.0</u>					
	<u>Fig. 4 III_b</u>	<u>0.39</u>	<u>0.63</u>	<u>1352</u>	<u>1875</u>	<u>6.9</u>	<u>0.28</u>	<u>0.65</u>	<u>~ 0.008</u>	<u>-0.21 ± 0.10</u>	<u>-0.22 ± 0.10</u>
<u>Loess Yingwang Plateau Shan</u>	<u>Fig. 5 I_a</u>	<u>0.54</u>	<u>0.21</u>	<u>1111</u>	<u>1224</u>	<u>5.8</u>			<u>0</u>	<u>~ 0.03</u>	<u>~ -0.01</u>
	<u>Fig. 5 I_b</u>	<u>0.20</u>	<u>0.32</u>	<u>1126</u>	<u>1225</u>	<u>5.0</u>	<u>0.21</u>	<u>0.31</u>	<u>0</u>	<u>~ 0.03</u>	<u>~ -0.01</u>
	<u>Fig. 5 II_a</u>	<u>0.24</u>	<u>0.36</u>	<u>1111</u>	<u>1257</u>	<u>7.4</u>			<u>0</u>	<u>~ 0.02</u>	<u>~ -0.01</u>
	<u>Fig. 5 II_b</u>	<u>0.30</u>	<u>0.31</u>	<u>1117</u>	<u>1224</u>	<u>5.4</u>	<u>0.39</u>	<u>0.33</u>	<u>0</u>	<u>~ 0.02</u>	<u>~ -0.01</u>
	<u>Fig. 5 III_a</u>	<u>0.29</u>	<u>0.46</u>	<u>1089</u>	<u>1256</u>	<u>8.6</u>			<u>0</u>	<u>~ 0.02</u>	<u>~ -0.01</u>
	<u>Fig. 5 III_b</u>	<u>0.56</u>	<u>0.37</u>	<u>1096</u>	<u>1203</u>	<u>5.3</u>	<u>0.49</u>	<u>0.35</u>	<u>0</u>	<u>~ 0.02</u>	<u>~ -0.01</u>

520 4. Discussion

521 4.1 Location of channel heads

522 Willett et al. (2014) pioneered the use of cross-divide χ contrast to gauge the
523 horizontal motion of drainage divides. According to their method, drainage divides
524 are predicted to move toward the side with a higher χ value to achieve geomorphic
525 equilibrium. However, in a region with spatially variable uplift rates, lithology, or
526 precipitation, χ contrast may fail to reflect the drainage-divide migration (Willett et
527 al., 2014; Whipple et al., 2017; Forte and Whipple, 2018; Wu et al., 2022; Zhou and
528 Tan, 2023). In ~~the a~~ tectonically active area, the cross-divide χ contrast can only be
529 used in a small area where rock type, precipitation, and uplift rate are nearly uniform
530 (Willett et al., 2014). ~~Forte and Whipple (2018) proposed the Gilbert metrics to~~
531 ~~measure the stability of drainage divides. Zhou et al. (2022a) combined eCombining~~
532 the advantages of the χ and Gilbert metrics methods, Zhou et al. (2022a) proposed to
533 use the χ contrast with a high base level to calculate the k_{sn} values at the channel heads
534 on both sides of a drainage divide, and quantified the migration rate of drainage
535 divides at the eastern margin of Tibet.

536 To reduce the cross-divide difference in uplift rate, precipitation, and rock
537 strength, ~~these the Gilbert metrics or χ -comparison method in Zhou et al.~~
538 ~~(2022a) methods~~ should compare the parameters of points (slope, relief, elevation, and
539 k_{sn}) on both sides of the divide as closely as possible. As the hillslope area (above the
540 channel head) does not follow Eq. 1 (Stoke and Dietrich, 2006; Stark, 2010; Braun et

541 al., 2018; Dahlquist et al., 2018)), the channel heads are the closest point to the divide,
542 following Eq. 1. Channel heads, therefore, are suitable for measuring the drainage-
543 divide stability with ~~the~~ parameters of the upstream drainage area and channel
544 gradient (Forte and Whipple, 2018; Zhou et al., 2022a; ~~this study~~). However, limited
545 by the resolution of DEM, the location of the channel heads ~~sometimes cannot always~~
546 be accurately identified. The channel head parameters for calculating the migration
547 rates isare usually usually based on empirical ~~parameters~~ values in the previous study
548 studies (e.g., $A_{cr} = 10^5 \text{ m}^2$ in Zhou et al. (2022a)), which may induce
549 uncertainties.~~which may introduce errors in the result of drainage divide stability.~~

550 In this study, we advocate the use of high-resolution DEM to determine a more
551 accurate position and related parameters of the channel head, ~~-. The use of UAVs to~~
552 obtain the local DEM has become highly efficient. ~~given that~~ ~~Because the use of UAVs~~
553 ~~to obtain the local DEM has become highly efficient.~~ We advance the theory to
554 calculate the drainage-divide migration rate based on the measured channel-head
555 parameters. ~~Because the use of UAVs to obtain the local DEM has become highly~~
556 efficient. With the help of the aerial photography of UAVs and the SfM techniques, it
557 is possible to~~one can~~ obtain the ~~sub-meter~~ high- resolution topography data of
558 drainage divides (Figs. 4A & 5A) and get the required parameters (including the exact
559 locations of the channel heads across the drainage divide) through topography
560 analysis, which could improve the quantitative research on the drainage-divide
561 migration. Furthermore, the method provides a new avenue to combine with
562 catchment-wide ^{10}Be erosion rate or low-temperature thermochronology data to

563 calculate the migration rate, which has great potentials ~~of for~~ application in places
564 where some variables are hard to be constrained.

565

566 **4.2 Cross-divide difference in the uplift rate of the channel heads**

567 Although the channel heads across the divide are very close on the spatial scale of
568 an orogenic belt, differential uplift between the channel heads (ΔU_{ch}) could still exist,
569 especially in a tilting horst, such as the Wutai Shan. The cross-divide difference in
570 uplift rate could impact the calculation of the migration rate of drainage divides (Zhou
571 et al., 2022a). ~~Although the differential uplift rate is usually small enough to be
572 ignored in some natural cases, its influence on the migration rate of drainage divides
573 should be taken into account theoretically (Zhou et al., 2022a).~~

574 In this study, we quantify the influence of the cross-divide difference in rock
575 uplift rate (ΔU_{ch}) on the calculation of the migration rate of drainage divides at the
576 Wutai Shan, benefiting from the available tectonic and chronological research
577 (Clinkscales et al., 2020) and the newly obtained high-resolution topographic data. In
578 the Wutai Shan horst, ΔU_{ch} across the drainage divide is ~~~0.004~~0.008 mm/yr. We
579 estimated the influence of ΔU_{ch} on the drainage-divide migration rate in ~~the~~this case
580 ~~study of the Wutai Shan~~, which can reduce the error theoretically. If ΔU_{ch} is ignored,
581 the drainage-divide migration rate would decrease by ~4% in the Wutai Shan case.
582 Although ~4% seems to be negligible, such a ratio will increase if the mountain belt is
583 narrower, the tilting uplift is stronger, or the divide is closer to the steady state (i.e.,

584 the migration rate is lower) (Whipple et al., 2017; Ye et al., 2022). In other words, the
585 differential uplift may play a significant influence on the measurement of drainage-
586 divide stability in some situations. ~~If we consider an extreme example: when where~~
587 the main drainage divide of a tilting mountain range (relatively narrow in width) is at
588 a steady state, the gradient, relief, and elevation of the channel heads (collectively
589 called “Gilbert metrics”) (Forte and Whipple, 2018)) will show a systematic cross-
590 divide difference in theory. In this case, the drainage divide would be considered
591 unstable if ΔU_{ch} were neglected. Therefore, ~~we suggested this study highlights that~~
592 ΔU_{ch} should be taken into account, either in a qualitative or a quantitative evaluation
593 of the stability of drainage divides using the parameters on the channel heads.

594

595 **4.3 Error Limitations and uncertainties**

596 This study developed the method to calculate the drainage-divide migration
597 rate based on the measured channel-head parameters. However, uncertainties still
598 exist because of the limitations of this technique. Firstly, we assume the erosion
599 coefficient (K) is the same on both sides of a drainage divide in the derivation of the
600 equations. If there are differences in rock erodibility or precipitation differences
601 across the divide, uncertainties should exist in the results. Secondly, the calculation of
602 the migration rates is based on the erosion rates at the channel area in this study.
603 However, the occurrence of drainage-divide migration is directly driven by the
604 differential erosion of the hillslope area across the divide, mainly via the processes
605 including landslide, collapse, and diffusion (Stoke and Dietrich, 2006; Stark, 2010;

606 Braun et al., 2018; Dahlquist et al., 2018). Such discontinuous processes in the
607 hillslope area make it challenging to constrain erosion rates over such short
608 timescales. Over a relatively longer timescale-period (i.e., spanning multiple seismic
609 and climatic cycles), the erosion rate at the channel head area in this study can be
610 comparable with that at the hillslope area (Hurst et al., 2012; Godard et al., 2020).

611 The accuracy of the data and parameters can also impact the reliability of the
612 results. Firstly, we use the typical values of $n = 1$ and $m/n = 0.45$ in the two natural
613 cases to calculate the migration rate. If the actual values largely deviate from the
614 assumption, the errors would exist be introduced into the results. For this reason, we
615 have added the cases of $m/n = 0.35$ and 0.55 in the in the sSupplementary mMaterials.
616 Further estimation of these values (Mudd et al., 2018) could improve the accuracy of
617 the results. Secondly, in the case study of the Wutai Shan, we refer to the geological
618 and low-temperature thermochronology studies, and assume assuming a 0.50 ± 0.25
619 mm/yr erosion rate ~~at~~ at the northern margin of the Wutai Shan (i.e., the footwall of
620 the North Wutai Shan fault). Combining with the present-day k_{sn} , we calculate the
621 erosion coefficient (K) and derive the range of migration rates of the drainage divide.
622 If the present-day erosion rate deviates from the assumption, the errors would exist be
623 inevitable in the results. Moreover, the horizontal and vertical errors of the DEM data,
624 as well as the calculation errors in slope, upstream area and channel steepness can
625 also affect the reliability of the results. In the case study of the Yingwang Shan, the
626 lush vegetation may bring errors to the DEM data based on the SfM technology. The
627 application of airborne light detection and ranging (LiDAR) technology may help

628 ~~reduce this error. In summary~~Nonetheless, despite the challenges in the accuracy of
629 the results at present is affected by many factors that present challenges, but we
630 believe this study provides a useful and important method to calculate the drainage
631 divide migration rate.Future studies should take these challenges into account and
632 overcome them.

633

634 5. Conclusions

635 We have developed a new method- (called the "channel-head-point" method here)
636 to calculate the migration rate of drainage divides based ~~up~~on channel-head
637 parameters. We have also improved the previously proposed "channel-head-segment
638 method" in the previous study (Zhou et al., 2022a) to adapt the theory to areas where
639 the parameters of channel-heads can be accurately determined.

640 ~~elevations of outlets and channel heads are different across the drainage divide.~~

641 Using the new methods and high-resolution topographic data, we determined the
642 exact locations of the channel heads on both sides of the drainage divide and
643 quantified the drainage-divide migration rates in two natural cases in North China
644 ~~(the~~ Wutai Shan in the Shanxi Rift ~~System~~, and ~~an unnamed mountain range~~the
645 Yingwang Shan in the Loess Plateau) ~~in North China~~. The migration rates of the study
646 sites in the Wutai Shan are ~~0.1021-0.1327~~ mm/yr (~~moving north~~westward). The rates
647 are close to zero in the Yingwang Shan~~Loess Plateau~~.

648 Based on the locations of the channel heads and the uplift gradient of the Wutai

649 Shanmountain, we calculated the cross-divide difference in the uplift rate at the
650 channel heads (ΔU_{ch}), which is taken into account in the calculation of the drainage-
651 divide migration rate for the first time. If ΔU_{ch} is overlooked, the drainage-divide
652 migration rate of the study sites in the Wutai Shan ~~would~~ will be ~~~4%~~ underestimated
653 by ~4%. ~~We suggest~~ Our study highlights that ΔU_{ch} should be considered ~~if one aims~~
654 ~~to~~ in the ~~assessment of the drainage divide~~ stability of drainage divides based on the
655 cross-divide difference in channel-head parameters.

656

657 **Data availability.** The analysis of data is based on the Matlab toolbox TAK (Forte
658 and Whipple, 2019) and TopoToolbox (Schwanghart and Scherler, 2014). The
659 topography data (ALOS DEM, 12.5 m resolution) is downloaded from the Alaska
660 Satellite Facility (ASF) Data Search (<https://search.asf.alaska.edu/>).

661 **Acknowledgements.** We would like to thank the eEditor Simon Mudd, the
662 reviewer Thomas Bernard, and an anonymous reviewer whose suggestions have
663 greatly improved the paper.

664 ~~Financial support.~~ **Financial support.** This study is supported by the CAS Pioneer
665 Hundred Talents Program (E2K2010010) and the Fundamental Research Funds for
666 the State Key Laboratory of Earthquake Dynamics (LED2021A02).

667 **Competing interests.** The authors declare that they have no conflict of interest.

668 **Author contributions.** XT and CZ contributed to the design of the research
669 scheme. CZ performed the geomorphic analyses. CZ, XT, and FS carried out field
670 data collection. CZ, XT, YL, and FS contributed to the text and reviewed the paper.

671

672 **References**

673 Authemayou, C., Brocard, G., Delcaillau, B., Molliex, S., Pedoja, K., Husson, L., et
674 al., 2018. Unraveling the roles of asymmetric uplift, normal faulting and
675 groundwater flow to drainage rearrangement in an emerging karstic landscape.
676 Earth Surface Processes and Landforms, 43(9), 1885-1898.

677 <https://doi.org/10.1002/esp.4363>

678 Beeson, H.W., McCoy, S.W., Keen-Zebert, A., 2017. Geometric disequilibrium of
679 river basins produces long-lived transient landscapes. Earth Planet Sc Lett 475,
680 34-43. <https://doi.org/10.1016/j.epsl.2017.07.010>

681 Bernard, T., Sinclair, H.D., Gailleton, B., Fox, M., 2021. Formation of Longitudinal
682 River Valleys and the Fixing of Drainage Divides in Response to Exhumation of
683 Crystalline Basement. Geophys Res Lett 48.

684 <https://doi.org/10.1029/2020gl092210>.

685 [Bian, S., Tan, X., Liu, Y., Fan, S., Gong, J., Zhou, C., Shi, F., Murphy, M.A., 2024.](#)

686 [Orographic rainfall drives the Himalaya drainage divide to move north.](#)

687 [Geomorphology, 108952. https://doi.org/10.1016/j.geomorph.2023.108952](#)

688 Bonnet, S., 2009. Shrinking and splitting of drainage basins in orogenic landscapes
689 from the migration of the main drainage divide. Nature Geoscience 2, 766-771.

690 <https://doi.org/10.1038/ngeo666>

691 Bookhagen, B., Strecker, M.R., 2012. Spatiotemporal trends in erosion rates across a

692 pronounced rainfall gradient: Examples from the southern Central Andes. Earth
693 Planet Sc Lett 327-328, 97-110. <https://doi.org/10.1016/j.epsl.2012.02.005>

694 Braun, J., 2018. A review of numerical modeling studies of passive margin
695 escarpments leading to a new analytical expression for the rate of escarpment
696 migration velocity. Gondwana Research 53, 209-224.
697 <https://doi.org/10.1016/j.gr.2017.04.012>

698 Burbank, D.W., Leland, J., Fielding, E., Anderson, R.S., Brozovic, N., Reid, M.R.,
699 Duncan, C., 1996. Bedrock incision, rock uplift and threshold hillslopes in the
700 northwestern Himalayas. Nature 379, 505–510. <https://doi.org/10.1038/379505a0>

701 [Burbank, D.W., Anderson, R.S., 2001. Tectonic Geomorphology. Blackwell Science,
702 Massachusetts p. 274.](#)

703 Chen, C.-Y., Willett, S.D., Christl, M., Shyu, J.B.H., 2021. Drainage basin dynamics
704 during the transition from early to mature orogeny in Southern Taiwan. Earth
705 Planet Sc Lett 562. <https://doi.org/10.1016/j.epsl.2021.116874>

706 Clark, M.K., Schoenbohm, L.M., Royden, L.H., Whipple, K.X., Burchfiel, B.C.,
707 Zhang, X., Tang, W., Wang, E., Chen, L., 2004. Surface uplift, tectonics, and
708 erosion of eastern Tibet from large-scale drainage patterns. Tectonics 23, 1-20.
709 <https://doi.org/10.1029/2002tc001402>

710 [Clift, P.D., Blusztajn, J., 2005. Reorganization of the western Himalayan river system
711 after five million years ago. Nature 438, 1001-1003.
712 <https://doi.org/10.1038/nature04379>](#)

713 Clinkscales, C., Kapp, P., Wang, H., 2020. Exhumation history of the north-central

714 Shanxi Rift, North China, revealed by low-temperature thermochronology. *Earth*
715 *Planet Sc Lett* 536, 116146. <https://doi.org/10.1016/j.epsl.2020.116146>

716 Clubb, F.J., Mudd, S.M., Milodowski, D.T., Hurst, M.D., Slater, L.J., 2014. Objective
717 extraction of channel heads from high-resolution topographic data. *Water*
718 *Resources Research* 50, 4283-4304. <https://doi.org/10.1002/2013wr015167>

719 Crosby, B.T., Whipple, K.X., 2006. Knickpoint initiation and distribution within
720 fluvial networks: 236 waterfalls in the Waipaoa River, North Island, New
721 Zealand. *Geomorphology* 82, 16-38.
722 <https://doi.org/10.1016/j.geomorph.2005.08.023>

723 Dahlquist, M.P., West, A.J., Li, G., 2018. Landslide-driven drainage divide migration.
724 *Geology* 46, 403-406. <https://doi.org/10.1130/g39916.1>

725 Deng, B., Chew, D., Mark, C., Liu, S., Cogné, N., Jiang, L., O'Sullivan, G., Li, Z., Li,
726 J., 2020. Late Cenozoic drainage reorganization of the paleo-Yangtze river
727 constrained by multi-proxy provenance analysis of the Paleo-lake Xigeda. *GSA*
728 *Bulletin*. <https://doi.org/10.1130/b35579.1>

729 DiBiase, R.A., Whipple, K.X., Heimsath, A.M., Ouimet, W.B., 2010. Landscape form
730 and millennial erosion rates in the San Gabriel Mountains, CA. *Earth Planet Sc*
731 *Lett* 289, 134-144. <https://doi.org/10.1016/j.epsl.2009.10.036>

732 Duvall, A., 2004. Tectonic and lithologic controls on bedrock channel profiles and
733 processes in coastal California. *J Geophys Res* 109.
734 <https://doi.org/10.1029/2003jf000086>

735 Forte, A.M., Whipple, K.X., 2018. Criteria and tools for determining drainage divide

736 stability. *Earth Planet Sc Lett* 493, 102–117.

737 <https://doi.org/10.1016/j.epsl.2018.04.026>

738 Forte, A.M., Whipple, K.X., 2019. Short communication: The Topographic Analysis
739 Kit (TAK) for TopoToolbox. *Earth Surface Dynamics* 7, 87–95.

740 <https://doi.org/10.5194/esurf-7-87-2019>

741 Forte, A.M., Yanites, B.J., Whipple, K.X., 2016. Complexities of landscape evolution
742 during incision through layered stratigraphy with contrasts in rock strength.
743 *Earth Surface Processes and Landforms* 41, 1736-1757.

744 <https://doi.org/10.1002/esp.3947>

745 Fu, B., 1989. Soil erosion and its control in the loess plateau of China. *Soil Use and*
746 *Management* 5, 76-82. <https://doi.org/10.1111/j.1475-2743.1989.tb00765.x>

747 Gallen, S.F., 2018. Lithologic controls on landscape dynamics and aquatic species
748 evolution in post-orogenic mountains. *Earth Planet Sc Lett* 493, 150-160.

749 <https://doi.org/10.1016/j.epsl.2018.04.029>

750 Godard, V., Dosseto, A., Fleury, J., Bellier, O., Siame, L., 2019. Transient landscape
751 dynamics across the Southeastern Australian Escarpment. *Earth Planet Sc Lett*
752 506, 397-406. <https://doi.org/10.1016/j.epsl.2018.11.017>

753 [Godard, V., Hippolyte, J.-C., Cushing, E., Espurt, N., Fleury, J., Bellier, O., Ollivier,](#)
754 [V., 2020. Hillslope denudation and morphologic response to a rock uplift](#)
755 [gradient. *Earth Surface Dynamics* 8, 221-243. \[https://doi.org/10.5194/esurf-8-\]\(https://doi.org/10.5194/esurf-8-221-2020\)](#)
756 [221-2020](#)

757 Goren, L., Fox, M., Willett, S.D., 2014. Tectonics from fluvial topography using

758 formal linear inversion: Theory and applications to the Inyo Mountains,
759 California. *Journal of Geophysical Research: Earth Surface* 119, 1651-1681.
760 <https://doi.org/10.1002/2014jf003079>

761 Hancock, G.S., Anderson, R.S., 2002. Numerical modeling of fluvial strath-terrace
762 formation in response to oscillating climate. *GSA Bulletin* 114, 1131-1142.
763 [https://doi.org/10.1130/0016-7606\(2002\)114<1131:nmofst>2.0.co;2](https://doi.org/10.1130/0016-7606(2002)114<1131:nmofst>2.0.co;2)

764 He, C., Yang, C.J., Turowski, J.M., Rao, G., Roda-Boluda, D.C., Yuan, X.P., 2021.
765 Constraining tectonic uplift and advection from the main drainage divide of a
766 mountain belt. *Nat Commun* 12, 544. [https://doi.org/10.1038/s41467-020-20748-](https://doi.org/10.1038/s41467-020-20748-2)
767 [2](https://doi.org/10.1038/s41467-020-20748-2)

768 Hilley, G.E., Arrowsmith, J.R., 2008. Geomorphic response to uplift along the
769 Dragon's Back pressure ridge, Carrizo Plain, California. *Geology* 36.
770 <https://doi.org/10.1130/g24517a.1>

771 [Hoorn, C., Wesselingh, F.P., Steege, H.T., Bermudez, M.A., Antonelli, A., 2010.](#)
772 [Amazonia Through Time: Andean Uplift, Climate Change, Landscape Evolution,](#)
773 [and Biodiversity. *Science* 330, 927-931. https://doi.org/10.1126/science.1194585](#)

774 [Hoskins, A.M., Attal, M., Mudd, S.M., Castillo, M., 2023. Topographic Response to](#)
775 [Horizontal Advection in Normal Fault-Bound Mountain Ranges. *Journal of*](#)
776 [Geophysical Research: Earth Surface](#) 128. <https://doi.org/10.1029/2023jf007126>.

777 Howard, A.D., Dietrich, W.E., Seidl, M.A., 1994. Modeling fluvial erosion on
778 regional to continental scales. *Journal of Geophysical Research: Solid Earth* 99,
779 13971-13986. <https://doi.org/10.1029/94jb00744>

780 Howard, A.D., Kerby, G., 1983. Channel changes in badlands. Geological Society of
781 America Bulletin 94, 739. [https://doi.org/10.1130/0016-](https://doi.org/10.1130/0016-7606(1983)94<739:CCIB>2.0.CO;2)
782 [7606\(1983\)94<739:CCIB>2.0.CO;2](https://doi.org/10.1130/0016-7606(1983)94<739:CCIB>2.0.CO;2)

783 Hu, K., Fang, X., Ferrier, K.L., Granger, D.E., Zhao, Z., Ruetenik, G.A., 2021.
784 Covariation of cross-divide differences in denudation rate and χ : Implications for
785 drainage basin reorganization in the Qilian Shan, northeast Tibet. Earth Planet Sc
786 Lett 562, 116812. <https://doi.org/10.1016/j.epsl.2021.116812>

787 [Hurst, M.D., Mudd, S.M., Walcott, R., Attal, M., Yoo, K., 2012. Using hilltop](#)
788 [curvature to derive the spatial distribution of erosion rates. Journal of](#)
789 [Geophysical Research: Earth Surface 117, n/a-n/a.](#)
790 <https://doi.org/10.1029/2011jf002057>

791 Jiao, R., Fox, M., Yang, R., 2022. Late Cenozoic erosion pattern of the eastern margin
792 of the Sichuan Basin: Implications for the drainage evolution of the Yangtze
793 River. Geomorphology 398, 108025.
794 <https://doi.org/10.1016/j.geomorph.2021.108025>

795 Kirby, E., Whipple, K., 2001. Quantifying differential rock-uplift rates via stream
796 profile analysis. Geology 29, 415-418. [https://doi.org/10.1130/0091-](https://doi.org/10.1130/0091-7613(2001)029<0415:Qdrurv>2.0.Co;2)
797 [7613\(2001\)029<0415:Qdrurv>2.0.Co;2](https://doi.org/10.1130/0091-7613(2001)029<0415:Qdrurv>2.0.Co;2)

798 [Kirby, E., Whipple, K., Tang, W., Chen, Z., 2003. Distribution of active rock uplift](#)
799 [along the eastern margin of the Tibetan Plateau: Inferences from bedrock channel](#)
800 [longitudinal profiles. Journal of Geophysical Research, 108\(B4\), 2217,](#)
801 [https://doi.org/10.1029/2001JB000861.](https://doi.org/10.1029/2001JB000861)

802 Kirby, E., Whipple, K.X., 2012. Expression of active tectonics in erosional
803 landscapes. *J Struct Geol* 44, 54-75. <https://doi.org/10.1016/j.jsg.2012.07.009>

804 Kirkpatrick, H.M., Moon, S., Yin, A., Harrison, T.M., 2020. Impact of fault damage
805 on eastern Tibet topography. *Geology* 48. <https://doi.org/10.1130/g48179.1>

806 Ma, Z., Zhang, H., Wang, Y., Tao, Y., Li, X., 2020. Inversion of Dadu River Bedrock
807 Channels for the Late Cenozoic Uplift History of the Eastern Tibetan Plateau.
808 *Geophys Res Lett* 47. <https://doi.org/10.1029/2019gl086882>

809 Mandal, S.K., Lupker, M., Burg, J.-P., Valla, P.G., Haghypour, N., Christl, M., 2015.
810 Spatial variability of ¹⁰Be-derived erosion rates across the southern Peninsular
811 Indian escarpment: A key to landscape evolution across passive margins. *Earth*
812 *Planet Sc Lett* 425, 154-167. <https://doi.org/10.1016/j.epsl.2015.05.050>

813 Molnar, P., England, P., 1990. Late Cenozoic uplift of mountain ranges and global
814 climate change: chicken or egg? *Nature* 346, 29-34.
815 https://doi.org/10.1038_346029a0

816 Mudd, S.M., Clubb, F.J., Gailleton, B., Hurst, M.D., 2018. How concave are river
817 channels? *Earth Surface Dynamics* 6, 505-523. [https://doi.org/10.5194/esurf-6-](https://doi.org/10.5194/esurf-6-505-2018)
818 [505-2018](https://doi.org/10.5194/esurf-6-505-2018)

819 Musher, L.J., Giakoumis, M., Albert, J., Rio, G.D., Rego, M., Thom, G., Aleixo, A.,
820 Ribas, C.C., Brumfield, R.T., Smith, B.T., 2021. River network rearrangements
821 promote speciation in lowland Amazonian birds. *Cold Spring Harbor Laboratory*.
822 <https://doi.org/10.1126/sciadv.abn1099>

823 Perron, J.T., Dietrich, W.E., Kirchner, J.W., 2008. Controls on the spacing of first-

824 order valleys. J Geophys Res 113. <https://doi.org/10.1029/2007jf000977>

825 Perron, J.T., Royden, L., 2013. An integral approach to bedrock river profile
826 analysis. Earth Surface Processes and Landforms 38, 570-576.
827 <https://doi.org/10.1002/esp.3302>

828 Pritchard, D., Roberts, G.G., White, N.J., Richardson, C.N., 2009. Uplift histories
829 from river profiles. Geophys Res Lett 36. <https://doi.org/10.1029/2009gl040928>

830 [Royden, L., Clark, M., Whipple, K., 2000. Evolution of river elevation profiles by](#)
831 [bedrock incision: Analytical solutions for transient river profiles related to](#)
832 [changing uplift and precipitation rates. Eos Trans. AGU 81.](#)

833 Safran, E.B., Bierman, P.R., Aalto, R., Dunne, T., Whipple, K.X., Caffee, M., 2005.
834 Erosion rates driven by channel network incision in the Bolivian Andes. Earth
835 Surface Processes and Landforms 30, 1007-1024.
836 <https://doi.org/10.1002/esp.1259>

837 Sassolas-Serrayet, T., Cattin, R., Ferry, M., Godard, V., Simoes, M., 2019. Estimating
838 the disequilibrium in denudation rates due to divide migration at the scale of
839 river basins. Earth Surface Dynamics 7, 1041-1057.
840 <https://doi.org/10.5194/esurf-7-1041-2019>

841 [Scheingross, J.S., Limaye, A.B., McCoy, S.W., Whittaker, A.C., 2020. The shaping of](#)
842 [erosional landscapes by internal dynamics. Nature Reviews Earth &](#)
843 [Environment 1, 661-676. https://doi.org/10.1038/s43017-020-0096-0](#)

844

845 Scherler, D., Schwanghart, W., 2020. Drainage divide networks – Part 2: Response to

846 perturbations. *Earth Surface Dynamics* 8, 261-274. <https://doi.org/10.5194/esurf->
847 [8-261-2020](https://doi.org/10.5194/esurf-8-261-2020)

848 Schildgen, T.F., van der Beek, P.A., D'Arcy, M., Roda-Boluda, D., Orr, E.N.,
849 Wittmann, H., 2022. Quantifying drainage-divide migration from orographic
850 rainfall over geologic timescales: Sierra de Aconquija, southern Central Andes.
851 *Earth Planet Sc Lett* 579, 117345. <https://doi.org/10.1016/j.epsl.2021.117345>

852 Schlunegger, F., Norton, K.P., Zeilinger, G., 2011. Climatic Forcing on Channel
853 Profiles in the Eastern Cordillera of the Coroico Region, Bolivia. *The Journal of*
854 *Geology* 119, 97-107. <https://doi.org/10.1086/657407>

855 Schwanghart, W., D., S., 2014. Short Communication: TopoToolbox 2 – MATLAB-
856 based software for topographic analysis and modeling in Earth surface sciences.
857 *Earth Surface Dynamics* 2, 1-7. <https://doi.org/10.5194/esurf-2-1-2014>

858 Shelef, E., Goren, L., 2021. The rate and extent of wind-gap migration regulated by
859 tributary confluences and avulsions. *Earth Surface Dynamics*, 9(4), 687-700.
860 <https://doi.org/10.5194/esurf-9-687-2021>

861 Shi, F., Tan, X., Zhou, C., Liu, Y., 2021. Impact of asymmetric uplift on mountain
862 asymmetry: Analytical solution, numerical modeling, and natural examples.
863 *Geomorphology* 389, 107862. <https://doi.org/10.1016/j.geomorph.2021.107862>

864 Shi, W., Dong, S., Hu, J., 2020. Neotectonics around the Ordos Block, North China: A
865 review and new insights. *Earth-Science Reviews* 200, 102969.
866 <https://doi.org/10.1016/j.earscirev.2019.102969>

867 Stark, C.P., 2010. Oscillatory motion of drainage divides. *Geophys Res Lett* 37.

868 <https://doi.org/10.1029/2009gl040851>

869 Stock, J.D., Dietrich, W.E., 2006. Erosion of steepland valleys by debris flows.
870 Geological Society of America Bulletin 118, 1125-1148.

871 <https://doi.org/10.1130/b25902.1>

872 Stokes, M.F., Larsen, I.J., Goldberg, S.L., McCoy, S.W., Prince, P.P., Perron, J.T.,
873 2023. The Erosional Signature of Drainage Divide Motion Along the Blue Ridge
874 Escarpment. Journal of Geophysical Research: Earth Surface 128.
875 <https://doi.org/10.1029/2022jf006757>

876

877 Struth, L., Teixell, A., Owen, L.A., Babault, J., 2017. Plateau reduction by drainage
878 divide migration in the Eastern Cordillera of Colombia defined by morphometry
879 and ¹⁰Be terrestrial cosmogenic nuclides. Earth Surface Processes and Landforms
880 42, 1155-1170. <https://doi.org/10.1002/esp.4079>

881 Su, P., He, H., Tan, X., Liu, Y., Shi, F., Kirby, E., 2021. Initiation and Evolution of the
882 Shanxi Rift System in North China: Evidence From Low-Temperature
883 Thermochronology in a Plate Reconstruction Framework. Tectonics 40.
884 <https://doi.org/10.1029/2020tc006298>

885 Su, Q., Wang, X., Lu, H., Xie, H., 2020. Dynamic Divide Migration as a Response to
886 Asymmetric Uplift: An Example from the Zhongtiao Shan, North China. Remote
887 Sensing 12. <https://doi.org/10.3390/rs12244188>

888 Tucker, G.E., Bras, R.L., 1998. Hillslope processes, drainage density, and landscape
889 morphology. Water Resources Research 34, 2751-2764.

890 <https://doi.org/10.1029/98wr01474>

891 Tucker, G.E., Slingerland, R., 1997. Drainage basin responses to climate change.

892 Water Resources Research 33, 2031-2047. <https://doi.org/10.1029/97wr00409>

893 Vacherat, A., Bonnet, S., Mouthereau, F., 2018. Drainage reorganization and divide

894 migration induced by the excavation of the Ebro basin (NE Spain). Earth Surface

895 Dynamics, 6(2), 369-387. <https://doi.org/10.5194/esurf-6-369-2018>

896 Wang, Y., Liu, C., Zheng, D., Zhang, H., Yu, J., Pang, J., Li, C., Hao, Y., 2021.

897 Multistage Exhumation in the Catchment of the Anninghe River in the SE

898 Tibetan Plateau: Insights From Both Detrital Thermochronology and

899 Topographic Analysis. Geophys Res Lett 48.

900 <https://doi.org/10.1029/2021gl092587>

901 [Waters, J.M., Craw, D., Youngson, J.H., Wallis, G.P., 2001. Genes meet geology: fish](https://doi.org/10.1111/j.0014-3820.2001.tb00833.x)

902 [phylogeographic pattern reflects ancient, rather than modern, drainage](https://doi.org/10.1111/j.0014-3820.2001.tb00833.x)

903 [connections. Evolution 55, 1844-1851. https://doi.org/10.1111/j.0014-](https://doi.org/10.1111/j.0014-3820.2001.tb00833.x)

904 [3820.2001.tb00833.x](https://doi.org/10.1111/j.0014-3820.2001.tb00833.x)

905

906 [Wei, Z., Arrowsmith, J.R., He, H., 2015. Evaluating fluvial terrace riser degradation](https://doi.org/10.1016/j.jseaes.2015.02.016)

907 [using LiDAR-derived topography: An example from the northern Tian Shan,](https://doi.org/10.1016/j.jseaes.2015.02.016)

908 [China. Journal of Asian Earth Sciences 105, 430-442.](https://doi.org/10.1016/j.jseaes.2015.02.016)

909 [https://doi.org/10.1016/j.jseaes.2015.02.016.](https://doi.org/10.1016/j.jseaes.2015.02.016)

910 Whipple, K.X., 2009. The influence of climate on the tectonic evolution of mountain

911 belts. Nature Geoscience 2, 97-104. <https://doi.org/10.1038/ngeo413>

912 Whipple, K.X., Forte, A.M., DiBiase, R.A., Gasparini, N.M., Ouimet, W.B., 2017.
913 Timescales of landscape response to divide migration and drainage capture:
914 Implications for the role of divide mobility in landscape evolution. *Journal of*
915 *Geophysical Research: Earth Surface* 122, 248-273.
916 <https://doi.org/10.1002/2016JF003973>

917 Whipple, K.X., Kirby, E., Brocklehurst, S.H., 1999. Geomorphic limits to climate-
918 induced increases in topographic relief. *Nature* 401, 39-43.
919 <https://doi.org/10.1038/43375>

920 Willett, S.D., McCoy, S.W., Perron, J.T., Goren, L., Chen, C.Y., 2014. Dynamic
921 reorganization of river basins. *Science* 343, 1117.
922 <https://doi.org/10.1126/science.1248765>

923 [Willett, S.D., McCoy, S.W., Beeson, H.W., 2018. Transience of the North American](#)
924 [High Plains landscape and its impact on surface water. *Nature* 561, 528-532.](#)
925 <https://doi.org/10.1038/s41586-018-0532-1>

926 Wobus, C., Whipple, K.X., Kirby, E., Snyder, N., Johnson, J., Spyropolou, K., Crosby,
927 B., Sheehan, D., 2006. Tectonics from topography: Procedures, promise, and
928 pitfalls, *Tectonics, Climate, and Landscape Evolution*, pp. 55-74.
929 [https://doi.org/10.1130/2006.2398\(04\)](https://doi.org/10.1130/2006.2398(04))

930 [Wu, Y., Yang, R., He, C., He, J., 2022. Caution on determining divide migration from](#)
931 [cross-divide contrast in \$\gamma\$. *Geological Journal* 57\(12\),](#)
932 [https://doi.org/10.1002/gj.4530.](https://doi.org/10.1002/gj.4530)

933 Xiong, L.-Y., Tang, G.-A., Li, F.-Y., Yuan, B.-Y., Lu, Z.-C., 2014. Modeling the

934 evolution of loess-covered landforms in the Loess Plateau of China using a DEM
935 of underground bedrock surface. *Geomorphology* 209, 18-26.
936 <https://doi.org/10.1016/j.geomorph.2013.12.009>

937 Xu, X., Ma, X., Deng, Q., 1993. Neotectonic activity along the Shanxi rift system,
938 China. *Tectonophysics* 219, 305-325. [https://doi.org/10.1016/0040-](https://doi.org/10.1016/0040-1951(93)90180-R)
939 [1951\(93\)90180-R](https://doi.org/10.1016/0040-1951(93)90180-R)

940 Yan, M.-J., He, Q.-Y., Yamanaka, N., Du, S., 2014. Location, Geology and Landforms
941 of the Loess Plateau, in: Tsunekawa, A., Liu, G., Yamanaka, N., Du, S. (Eds.),
942 Restoration and development of the degraded Loess Plateau, China. Springer
943 Japan, pp. 3-22. <https://doi.org/10.1007/978-4-431-54481-4>

944 Yang, R., Suhail, H.A., Gourbet, L., Willett, S.D., Fellin, M.G., Lin, X., Gong, J., Wei,
945 X., Maden, C., Jiao, R., Chen, H., 2019. Early Pleistocene drainage pattern
946 changes in Eastern Tibet: Constraints from provenance analysis,
947 thermochronometry, and numerical modeling. *Earth Planet Sc Lett* 531, 1-10.
948 <https://doi.org/10.1016/j.epsl.2019.115955>

949 Ye, Y., Tan, X., Zhou, C., 2022. Initial topography matters in drainage divide
950 migration analysis: Insights from numerical simulations and natural examples.
951 *Geomorphology* 409, 108266. <https://doi.org/10.1016/j.geomorph.2022.108266>

952 Yin, A., 2010. Cenozoic tectonic evolution of Asia: A preliminary synthesis.
953 *Tectonophysics* 488, 293-325. <https://doi.org/10.1016/j.tecto.2009.06.002>

954 [Zemlak, T.S., Habit, E.M., Walde, S.J., Battini, M.A., Adams, E.D.M., Ruzzante,](#)
955 [D.E., 2008. Across the southern Andes on fin: glacial refugia, drainage reversals](#)

956 [and a secondary contact zone revealed by the phylogeographical signal of](#)
957 [Galaxias platei in Patagonia. *Molecular Ecology* 17, 5049-5061.](#)
958 <https://doi.org/10.1111/j.1365-294X.2008.03987.x>

959 Zeng, X., Tan, X., 2023. Drainage divide migration in response to strike-slip faulting:
960 An example from northern Longmen Shan, eastern Tibet. *Tectonophysics* 848,
961 229720. <https://doi.org/10.1016/j.tecto.2023.229720>

962 Zhao, X., Zhang, H., Hetzel, R., Kirby, E., Duvall, A.R., Whipple, K.X., Xiong, J., Li,
963 Y., Pang, J., Wang, Y., Wang, P., Liu, K., Ma, P., Zhang, B., Li, X., Zhang, J.,
964 Zhang, P., 2021. Existence of a continental-scale river system in eastern Tibet
965 during the late Cretaceous-early Palaeogene. *Nat Commun* 12, 7231.
966 <https://doi.org/10.1038/s41467-021-27587-9>

967 Zhou, C., Tan, X., Liu, Y., Lu, R., Murphy, M.A., He, H., Han, Z., Xu, X., 2022a.
968 Ongoing westward migration of drainage divides in eastern Tibet, quantified
969 from topographic analysis. *Geomorphology* 402, 108123.
970 <https://doi.org/10.1016/j.geomorph.2022.108123>

971 Zhou, C., Tan, X., Liu, Y., Shi, F., 2022b. A cross-divide contrast index (C) for
972 assessing controls on the main drainage divide stability of a mountain belt.
973 *Geomorphology* 398, 108071. <https://doi.org/10.1016/j.geomorph.2021.108071>.

974 Zhou, C., Tan, X., 2023. Quantifying the influence of asymmetric uplift, base level
975 elevation, and erodibility on cross-divide χ difference. *Geomorphology* 427,
976 108634. <https://doi.org/10.1016/j.geomorph.2023.108634>

977 Zondervan, J.R., Stokes, M., Boulton, S.J., Telfer, M.W., Mather, A.E., 2020. Rock

978 strength and structural controls on fluvial erodibility: Implications for drainage
979 divide mobility in a collisional mountain belt. Earth Planet Sc Lett 538.
980 <https://doi.org/10.1016/j.epsl.2020.116221>